Research Square

Preprints are preliminary reports that have not undergone peer review.
They should not be considered conclusive, used to inform clinical practice,
or referenced by the media as validated information.

Experimental evaluation and GC–MS guided computational identification of potential antidiabetic compounds from Heritiera fomes leaves

Arghya Prosun Sarkar
Islamic University
Musab Shahariar
mshahariar20@gmail.com
Islamic University
Lamia Hasan Barsha Joarder
Islamic University
Naem Islam Abhi Sheikh
Islamic University
Md. Abdullah Al Mashud
Greenford Nano and Cancer Foundation
Panna Roy
Jahangirnagar University
Arjyabrata Sarker
Jahangirnagar University
Farhana Islam
Jashore University of Science and Technology
Md. Rezaul Karim
Islamic University
Muhammad Shamsuzzaman
National Institute of Biotechnology
Mst. Muslima Khatun
National Institute of Biotechnology
Sukalyan Kumar Kundu
Jahangirnagar University

Research Article

Keywords: Type 2 diabetes mellitus (T2DM), Oxidative stress, Inflammation, FTIR, GCñMS, Molecular docking, ADMET, DFT, MD simulation

Posted Date: May 26th, 2026

DOI: https://doi.org/10.21203/rs.3.rs-9524528/v1

License: This work is licensed under a Creative Commons Attribution 4.0 International License.
Read Full License

Additional Declarations: No competing interests reported.

Experimental evaluation and GC–MS guided computational identification of potential antidiabetic compounds from *Heritiera fomes* leaves

Arghya Prosun Sarkar[1,2], Musab Shahariar[1*], Lamia Hasan Joarder Barsha[1†], Sheikh Naem Islam Abhi[1†], Md. Abdullah Al Mashud[2,3*], Panna Roy[4], Arjyabrata Sarker[4,5], Farhana Islam[6], Md. Rezaul Karim[7], Muhammad Shamsuzzaman[8], Mst. Muslima Khatun[9], and Sukalyan Kumar Kundu[4*]

[1]Department of Pharmacy, Faculty of Biological Sciences, Islamic University, Kushtia-7003, Bangladesh.

[2]Greenford Nano and Cancer Foundation, Kushtia-7000, Bangladesh.

[3]Biophysics and Biomedicine Research Lab, Department of Electrical and Electronic Engineering, Islamic University, Kushtia-7003, Bangladesh.

[4]Department of Pharmacy, Jahangirnagar University, Savar, Dhaka-1342, Bangladesh.

[5]Strategic Brand Management Department, Beximco Pharmaceuticals PLC., 19 Dhanmondi R/A, Road No.07, Dhaka-1205, Bangladesh.

[6]Department of Pharmacy, Jashore University of Science and Technology, Jashore-7408.

[7]Department of Biotechnology and Genetic Engineering, Faculty of Biological Sciences, Islamic University, Kushtia-7003, Bangladesh.

[8]Scientific Officer, Molecular Biotechnology Division, National Institute of Biotechnology, Ganakbari, Ashulia, Savar, Dhaka-1349

[9]Senior Scientific Officer, Molecular Biotechnology Division, National Institute of Biotechnology, Ganakbari, Ashulia, Savar, Dhaka-1349

†These authors contributed equally to this study

*Correspondence: Musab Shahariar (mshahariar20@gmail.com), Md. Abdullah Al Mashud (mashud.eap@gmail.com), Sukalyan Kumar Kundu (skkbd415@juniv.edu)

Abstract

Background: Type 2 diabetes mellitus is a chronic metabolic disorder characterized by insulin resistance and progressive pancreatic β-cell dysfunction, with an increasing global burden. The limitations of existing therapies, particularly their adverse effects and suboptimal long-term efficacy, underscore the need for safer and more effective antidiabetic agents. Phytochemicals represent a valuable reservoir for novel drug discovery. Mangrove species represent promising yet insufficiently explored sources of bioactive phytochemicals.

Methods: Following plant material collection and extract preparation, qualitative and quantitative phytochemical characterization was performed. Antioxidant activity was assessed via DPPH free radical scavenging and ferricyanide reducing power assays. Anti-inflammatory potential was determined through bovine serum and egg albumin denaturation inhibition assays. Antidiabetic activity was evaluated in vitro using α-amylase and α-glucosidase inhibition assays. Prior to in vivo studies, the extract's safety profile was established through invertebrate and mammalian toxicity models. Antihyperglycemic efficacy was subsequently assessed using the oral glucose

tolerance test (OGTT) and an alloxan-induced diabetic rat model. Metabolite profiling was conducted by FTIR and GC–MS analyses. Identified bioactive constituents were further subjected to molecular docking, ADMET profiling, density functional theory (DFT) calculations, and molecular dynamics (MD) simulations to prioritize lead candidates for antidiabetic drug development.

Results: The extract exhibited significant antioxidant and anti-inflammatory activities and demonstrated potent inhibition of α-amylase (IC_{50} = 40.07 ± 0.18 µg/mL) and α-glucosidase (IC_{50} = 35.75 ± 1.42 µg/mL), surpassing that of acarbose. Toxicological assessment revealed moderate cytotoxicity in the brine shrimp assay and low acute toxicity in vivo. In oral glucose tolerance and alloxan-induced diabetic models, the extract significantly improved glucose tolerance and reduced chronic hyperglycemia, outperforming metformin. FTIR analysis enabled functional group characterization, whereas GC–MS facilitated the identification of individual constituents, leading to the detection of 97 secondary metabolites. Comprehensive computational screening, including molecular docking, ADMET prediction, density functional theory-based reactivity assessment, and 100 ns molecular dynamics simulations, identified compounds 61, 78, and 88 as promising candidates.

Conclusion: Collectively, these findings establish *H. fomes* leaves as a promising natural source for the discovery of potential antidiabetic agents and further pharmacological development.

Keywords: Type 2 diabetes mellitus (T2DM), Oxidative stress, Inflammation, FTIR, GC–MS, Molecular docking, ADMET, DFT, MD simulation

1. Introduction

Diabetes mellitus (DM) encompasses a group of prevalent metabolic disorders characterized by persistent hyperglycemia [1]. It is classified into type 1 diabetes mellitus (T1DM), type 2 diabetes mellitus (T2DM), specific forms of diabetes, and gestational diabetes mellitus. T2DM is a nonautoimmune, heterogeneous, and progressive disorder marked by inadequate pancreatic islet β-cell insulin secretion. T2DM commonly occurs in the presence of insulin resistance (IR) and is frequently associated with metabolic syndrome [2]. Globally, approximately 11.1% of adults are affected by diabetes, with more than 90% being diagnosed with T2DM [3], underscoring its substantial public health impact. T2DM is associated with microvascular complications and macrovascular events, as well as heart failure and nonalcoholic fatty liver disease (NAFLD). Emerging evidence also links diabetes to cognitive decline and Alzheimer's disease. Cumulative data indicate a strong interplay among chronic hyperglycemia, oxidative stress, and inflammation in driving T2DM progression and its associated complications [4, 5]. These complications substantially reduce quality of life and increase premature mortality [4]. The current therapeutic landscape for T2DM encompasses a diverse range of approved pharmacological agents that target multiple pathophysiological mechanisms [6]. These include biguanides, sulfonylureas, thiazolidinediones, dipeptidyl peptidase-4 (DPP-4) inhibitors, glucagon-like peptide-1 (GLP-1) receptor agonists, sodium–glucose cotransporter 2 (SGLT2) inhibitors, insulin, meglitinides, and α-glucosidase and α-amylase inhibitors [7–9]. The inhibition of intestinal α-amylase and α-glucosidase reduces postprandial hyperglycemia by delaying carbohydrate digestion and glucose absorption, which represents an established strategy particularly in early-stage diabetes [10]. Agents such as acarbose and miglitol are effective but commonly cause gastrointestinal adverse effects [9]. Additionally, current therapies are limited by risks including hypoglycemia, weight

gain, edema, cost, and declining long-term efficacy, underscoring the need for safer and more durable treatment options [7, 8, 11].

Medicinal plants, which are widely utilized in traditional systems of medicine, have long been employed for the management of various disorders, including diabetes [12, 13]. Diverse classes of plant-derived secondary metabolites exhibit antihyperglycemic activity through multiple mechanisms, including the inhibition of α-amylase and α glucosidase [10, 13]. Emerging evidence suggests that these phytochemicals may offer effective glycemic control with comparatively favorable safety profiles [14]. Among plant-derived bioactive compounds, phenolic constituents have emerged as particularly promising because their potent antidiabetic effects are mediated through distinct structure-dependent mechanisms [15]. In addition to their ability to inhibit α-amylase and α-glucosidase, phenolic compounds demonstrate significant antioxidant and anti-inflammatory activities, underscoring their therapeutic potential in mitigating diabetes and its associated complications [16]. Collectively, these findings underscore the potential of plant-derived secondary metabolites as promising lead compounds for the development of potent and safer antidiabetic therapeutics.

Bangladesh harbors the Sundarbans, the world's largest contiguous mangrove forest, where local and indigenous communities, including the Munda population, depend extensively on mangrove and mangrove-associated flora for primary healthcare [17]. At least 41 documented species are traditionally used to manage digestive, dermatological, respiratory, metabolic, and sociocultural disorders, underscoring their ethnopharmacological significance and potential for drug discovery [17]. Mangrove plants endure extreme environmental stresses like high salinity, hypoxia, and tidal fluctuations, which drive the biosynthesis of structurally unique secondary metabolites, including terpenoids, limonoids, and complex polyphenols with reported antidiabetic, antioxidant, and anti-

inflammatory activities [18]. However, on a global scale, only approximately one-third of mangrove species have undergone pharmacological evaluation, and an even smaller proportion have been subjected to comprehensive phytochemical characterization [19]. These observations underscore the potential of unexplored mangrove-derived phytochemicals to serve as lead scaffolds for the development of antidiabetic therapeutics. *Heritiera fomes* Buch. -Ham. (family: Sterculiaceae), commonly known as Sundari in Bengali, is a dominant and ecologically significant mangrove species distributed throughout the Sundarbans forest in southern Bangladesh and the adjoining region of West Bengal, India [20]. The plant holds substantial ethnomedicinal importance and has long been utilized in traditional folk medicine by local communities and traditional healers for the management of diabetes, hepatic and gastrointestinal disorders, goiter, and various dermatological conditions [20]. A limited number of experimental investigations have reported its potential antidiabetic activity on the basis of in vitro and in vivo studies [21, 22]. However, despite these preliminary findings, comprehensive metabolite profiling of *H. fomes* leaves and systematic identification of bioactive lead compounds relevant to diabetes and its associated complications remain largely unexplored. Accordingly, the present study adopted a multidisciplinary experimental framework to evaluate the antioxidant, anti-inflammatory, and antidiabetic properties of *H. fomes* leaves. This was followed by detailed phytochemical characterization via FTIR and GC–MS analyses. Furthermore, an integrated in silico approach comprising molecular docking, ADMET prediction, density functional theory (DFT), and molecular dynamics (MD) simulations was employed to identify potential *H. fomes* leaves-derived lead compounds that target α-amylase and α glucosidase.

2. Methodology

2.1 Collection, identification, preparation and extraction of the plant material

Leaves of *H. fomes* were collected from the Karamjol area of the Sundarbans mangrove forest, where the species is abundant. The plant was taxonomically identified at the Jahangirnagar University Herbarium (JUH), Dhaka (accession no. JUH 10429), and further verified using standard botanical literature. Identification was performed by Mr. Mohammad Abdur Rahim, Principal Experimental Officer, Department of Botany, Jahangirnagar University. The collected leaves were washed, shade-dried for seven days, oven-dried at 65°C, and pulverized [23, 24]. Approximately 1 kg of powdered material was extracted with methanol (2.5 L) by cold maceration for 48 h in a Soxhlet apparatus. The solvent was efficiently and carefully removed from the samples via a rotary evaporator, and the crude extract was stored at 4°C [25].

2.2 Chemicals and reagents

HPLC-grade methanol (Daejung Chemicals, South Korea) was used for extraction, and DPPH was obtained from TCI, Japan. All other analytical-grade reagents were purchased from commercial suppliers in India. Metformin hydrochloride (API) was procured from BEACON Pharmaceuticals PLC., Bangladesh.

2.3 Experimental animals

Female Sprague–Dawley rats (120–180 g) and Swiss albino mice (25–30 g) were obtained from the Department of Pharmacy, Jahangirnagar University, Dhaka, Bangladesh. The animals were housed in standard polypropylene cages under controlled laboratory conditions (12 h light/dark cycle; temperature 22 ± 3°C) with free access to standard commercial pellet diet and water ad libitum [26]. All experimental procedures were conducted in accordance with institutional ethical

guidelines and were approved by the Animal Welfare and Experimentation Ethics Committee, Faculty of Biological Sciences, Islamic University, Kushtia-7003, Bangladesh (Reference number: AWEEC/FOB/IU/2025(12)), ensuring compliance with ethical and biosafety standards throughout the study.

2.4 Qualitative and quantitative estimation of bioactive compounds

Preliminary phytochemical screening of the methanolic extract of *H. fomes* leaves (MEHFL) was conducted to qualitatively assess the presence of phenols, flavonoids, terpenoids, tannins, anthraquinones, reducing sugars, saponins, and steroids via standard procedures [27, 28] (Table 1). The quantitative estimation of total phenols, flavonoids, and tannins was performed spectrophotometrically using appropriate standards, and results were expressed as equivalents per gram of standards (Mean ± SEM). Total phenolic content (TPC) and total tannin content (TTC) were determined via the Folin–Ciocalteu method [29, 30] with gallic acid, whereas the total flavonoid content (TFC) was measured via the aluminum chloride assay with quercetin as the standard [30].

Table 1: Test methods and observations of qualitative phytochemical screening of methanolic extract of *H. fomes* leaves (MEHFL) [27, 28].

Phytochemical class	Test	Observation
Phenol	Potassium dichromate test	Dark color
Flavonoid	Ammonia test	Yellow color
Terpenoid	Salkowski's test	Grey color solution
Tannin	Braymer's test	Blue-green color
Anthraquinone	Borntrager's test	Pink, violet or red color solution
Reducing sugar	Benedict's test	Green, yellow or red color
Saponin	Olive oil test	Foam formation
Steroid	Acetic anhydride test	Change in color; violet to blue/green

2.5 In vitro antioxidant assays

2.5.1 DPPH free radical scavenging assay

The antioxidant activity of MEHFL was evaluated using the 2,2-diphenyl-1-picrylhydrazyl (DPPH) free radical scavenging assay with slight modifications [31]. Extracts (20–200 μg/mL) were reacted with 0.1 mM DPPH, and the absorbance was measured at 517 nm after 30 min. Ascorbic acid served as the positive control. The percent inhibition and IC_{50} values were determined from triplicate assays.

2.5.2 Ferricyanide reducing power assay

The reducing power of MEHFL was assessed via the ferricyanide assay [32]. The extract (12.5–400 μg/mL) reduced Fe^{3+} to Fe^{2+}, forming a ferric–ferrous complex measured at 700 nm. An increased absorbance indicates a greater reducing capacity. Ascorbic acid served as the positive control, and the assays were performed in triplicate.

2.6 In vitro anti-inflammatory assays

2.6.1 Bovine serum albumin denaturation (BSA) assay

The anti-inflammatory activity of MEHFL was evaluated by inhibition of BSA denaturation at concentrations ranging from 125–2000 μg/mL. The reaction mixtures were incubated and heat-induced denaturation was measured at 660 nm. Aspirin served as the positive control. The percent inhibition and IC_{50} values were determined from triplicate assays [33].

2.6.2 Egg albumin denaturation assay

The anti-inflammatory activity of MEHFL was also assessed by inhibition of egg albumin denaturation. The extract or diclofenac (125–2000 μg/mL) was incubated with egg albumin and

phosphate buffer, followed by heat-induced denaturation. The absorbance was measured at 660 nm. The percent inhibition and IC_{50} values were determined from triplicate assays [34].

2.7 In vitro antidiabetic assays

2.7.1 α-Amylase inhibition assay

The α-amylase inhibitory activity of MEHFL was evaluated via a modified McCue and Shetty method [35]. Extracts (12.5–400 µg/mL) were incubated with the α-amylase and starch substrates, and the absorbance was measured at 540 nm after DNSA (3,5-dinitrosalicylic acid) reaction. Acarbose served as the positive control, and the IC_{50} values were determined.

2.7.2 α-Glucosidase inhibition assay

The α-glucosidase inhibitory activity of MEHFL (12.5–400 µg/mL) was evaluated using pNPG (4-Nitrophenyl α-D-glucopyranoside) as a substrate [36]. The reaction mixtures were incubated with α glucosidase, and absorbance was measured at 405 nm after termination. Acarbose served as the positive control. The percentage inhibition and IC_{50} values were determined from triplicate assays.

2.8 Toxicological assessment

2.8.1 Brine shrimp lethality bioassay

The brine shrimp lethality bioassay was conducted using a 20,000 µg/mL stock solution of the extract in Dimethyl sulfoxide (DMSO), followed by serial dilutions (12.5–400 µg/mL) in simulated seawater (38 ppt). Potassium dichromate served as the control. Fifteen nauplii per tube were incubated for 24 h, and mortality was recorded. LC_{50} values were calculated from percentage mortality data [37, 38].

2.8.2 Acute oral toxicity study in mouse model

The acute oral toxicity of MEHFL was evaluated in female mice according to OECD guideline 423 [39]. A single oral dose of 5000 mg/kg body weight of the MEHFL, suspended in distilled water, was administered to the MEHFL group (n=5), whereas the control group (n=5) received distilled water only. Dosing was performed after an overnight fasting period, with food provided approximately 1 h post administration. The animals were monitored daily for 14 days to assess mortality, physical appearance, and clinical signs of toxicity, with body weights recorded at weekly intervals.

2.9 In vivo antidiabetic assays

2.9.1 Oral glucose tolerance test (OGTT) in nondiabetic mice

Following an overnight fast (12 h), the mice were administered a 40% glucose solution (2 g/kg) via oral gavage. The samples were randomly allocated into four groups (n =5): negative control (distilled water), positive control (metformin, 100 mg/kg), and treatment groups receiving MEHFL at 250 and 500 mg/kg. Blood glucose levels were measured via a Call EZ II glucometer (Acon Laboratories, Inc., San Diego, USA) via tail vein sampling at 0 min (prior to glucose administration), and subsequently at 30, 60, 90, and 120 min [40].

2.9.2 Assessment of fasting blood glucose (FBG) levels in alloxan-induced diabetic rats

The rats were fasted prior to diabetes induction with a single intraperitoneal injection of alloxan monohydrate (150 mg/kg) [41] and were maintained for 7 days with free access to food and water. After 7 days followed by a 12 h fasting period, fasting blood glucose (FBG) was measured in tail vein blood using a Call EZ II glucometer (Acon Laboratories, Inc., San Diego, USA), and samples with FBG ≥ 11 mmol/L were considered diabetic [42]. The rats were randomly assigned to five

groups (n = 5): normal control (nondiabetic; distilled water), negative control (diabetic; distilled water), positive control (diabetic; metformin 100 mg/kg), and MEHFL-treated (diabetic; 250 and 500 mg/kg). Treatments were administered orally for 21 days. FBG levels were recorded on days 1, 7, 14, and 21 following a 6-h fast.

2.10 Statistical analysis

The experimental data are expressed as the mean ± standard error of the mean (SEM) for the indicated number of experiments. Statistical analyses were performed using RStudio (R v4.4.0). Normality and homogeneity of variances were assessed using the Shapiro–Wilk and Levene's tests, respectively. Group differences were analyzed by one-way ANOVA followed by Dunnett's post hoc test, with $p < 0.05$ considered statistically significant [43].

2.11 Characterization and identification of phytoconstituents

2.11.1 Fourier-Transform Infrared (FTIR) spectroscopy analysis

The FTIR spectrum of MEHFL was recorded using an FTIR spectrophotometer (IRPrestige-21, Shimadzu, Japan) equipped with a deuterated L-alanine doped triglycine sulphate (DLATGS or DLTGS) detector, connected to IRSolution 1.40 software. Approximately 10 mg of the plant powder was thoroughly mixed with half a microspatula of chromatographic-grade potassium bromide (KBr) and compressed into a pellet. Spectra were acquired in the range of 4000–400 cm^{-1} at a resolution of 4 cm^{-1} by averaging 10 scans, using the potassium bromide (KBr) pellet method [44, 45].

2.11.2 Gas Chromatography–Mass Spectrometry (GC–MS) profiling

GC–MS analysis was performed using a Thermo Scientific™ TSQ™ 9000 Triple Quadrupole GC–MS/MS system coupled with a Thermo Scientific™ ISQ™ 7000 single quadrupole mass spectrometer. Separation was achieved on a TG-5MS capillary column (30 m × 0.25 mm i.d., 1 μm film thickness). The oven program was set from 60°C (5 min) to 180°C, then to 280°C, and finally to 310°C (3 min). A 1 μL sample was injected in split mode at 280°C, with helium as the carrier gas (1.2 mL/min). The total run time was 39.99 min, and compound identification was based on National Institute of Standard and Technology (NIST) library matching [45].

2.12 In silico analysis

2.12.1 Ligand retrieval and preparation

Following GC–MS analysis, the identified phytochemicals were subjected to computational characterization (Additional file 2, Table ST13). Along with the control compound (Acarbose), the three-dimensional molecular structures of the identified compounds were retrieved from the PubChem in SDF format. For certain compounds whose structures were not available in the PubChem database, ChemDraw 16 software was utilized to manually generate the chemical structures and their corresponding SMILES notations, which were then used for subsequent computational processing [46]. All the structures were modified and geometrically optimized using Gaussian 09 software, employing Density Functional Theory (DFT) with the B3LYP functional and the 6-311G(d,p) basis set [47].

2.12.2 Protein structure preparation, validation and active site prediction

The target proteins selected for computational studies were chosen based on their therapeutic relevance in diabetes management. α-amylase (PDB ID: 2QV4) [48] and α-glucosidase (PDB ID:

3A4A) [49] are key enzymes involved in carbohydrate metabolism and are widely recognized as validated targets for the development of antidiabetic agents [50, 51]. The three-dimensional crystal structures of these proteins were retrieved from the Protein Data Bank with resolutions ranging between 2.0 and 2.5 Å to ensure structural accuracy [52]. Following retrieval, the proteins were preprocessed using Discovery Studio 2024, and subsequently energy-minimized using SWISS-PDBViewer to relieve steric clashes and stabilize atomic positions [53]. The quality of the optimized protein structures was validated using web-based tools including SAVES v6.1 (ERRAT, VERIFY, and PROCHECK) and ProSA-Web [54, 55]. Putative ligand-binding sites were predicted using the PrankWeb server [56].

2.12.3 Molecular docking and interaction analysis

Molecular docking was performed using PyRx [57]. For α amylase, the grid box was centered at (16.567, 50.278, 26.078) with dimensions of 33.022 × 20.190 × 24.871 Å, whereas for α-glucosidase the center was set at (−15.000, −30.991, 96.062) with dimensions of 21.698 × 20.690 × 21.373 Å. The grids encompassed the predicted binding pockets to enable accurate protein–ligand interaction analysis. Docking poses were ranked according to binding affinity (kcal/mol), and compounds exhibiting binding energies equal to or stronger than the control were initially shortlisted. Two-dimensional interaction profiles and hydrogen bond analyses were generated using BIOVIA Discovery Studio 2024, while three-dimensional view of protein–ligand interactions were generated using PyMOL (v4.6.0) [58]. Compounds demonstrating favorable binding affinities and a higher number of direct hydrogen bonds with the target proteins were selected for subsequent computational analyses.

2.12.4 Evaluation of physicochemical, drug-likeliness and pharmacokinetic properties

Following molecular docking and interaction analyses, the selected compounds were assessed for their physicochemical, drug-likeness, pharmacokinetic (ADME: Absorption, Distribution, Metabolism, and Excretion), and toxicological properties. Canonical SMILES representations of the compounds were used as input for computational prediction platforms, including SwissADME, ADMETLab 2.0, Deep-PK, and ProTox3.0 to evaluate their physicochemical characteristics and ADMET profiles [59].

2.12.5 Assessment of passive permeability

The ability of the selected compounds to permeate the plasma membrane was evaluated using the PerMM web server. Optimized PDB structures of the compounds were submitted as input under default experimental settings. The server predicts membrane binding affinities, energy barriers along the membrane normal, and permeability coefficients [60, 61].

2.12.6 Off-target effects prediction

Swiss Target Prediction web tool was employed to identify potential off-target interactions of the selected compounds. Canonical SMILES representations were used as input for the analysis, and predicted targets were ranked by probability scores ranging from 0 to 1, with values closer to 1 indicating a higher likelihood of interaction between the compound and the predicted target [62].

2.12.7 Quantum chemical reactivity analysis

Quantum chemical reactivity analysis of the selected compounds was performed using density functional theory (DFT) at the B3LYP/6-311G(d,p) level with Gaussian 09 [47, 63]. Reactivity-

and stability-related descriptors were visualized and analyzed using GaussView 5 and calculated according to the following equations:

$$E_{gap} = (E_{LUMO} - E_{HOMO}) \dots\dots\dots (i)$$

$$I = -E_{LUMO} \dots\dots\dots (ii)$$

$$A = -E_{HOMO} \dots\dots\dots (iii)$$

$$\mu = -\frac{(I + A)}{2} \dots\dots\dots (iii)$$

$$\chi = \frac{(I + A)}{2} \dots\dots\dots (iv)$$

$$\varpi^2 = \frac{\mu^2}{2\eta} \dots\dots\dots (v)$$

$$\eta = \frac{I - A}{2} \dots\dots\dots (vi)$$

$$\sigma = \frac{1}{\eta} \dots\dots\dots (vii)$$

where E_{gap} denotes the energy gap; E_{LUMO} the lowest unoccupied molecular orbital; E_{HOMO} the highest occupied molecular orbital; I the ionization potential; A the electron affinity; μ the chemical potential; χ the electronegativity; ω the electrophilicity index; η the chemical hardness; and σ the chemical softness.

2.12.8 Molecular dynamics simulation and post-simulation analysis

Molecular dynamics (MD) simulations were performed to investigate the conformational stability and dynamic properties of protein–ligand complexes within the target binding sites. Simulations

were carried out for 100 ns using the Desmond v3.6 module (Schrödinger suite) under a Linux environment, employing the OPLS_3e force field [64]. Complexes were solvated in an orthorhombic box with TIP3P water and a 10 Å buffer, neutralized with Na^+/Cl^- ions at 0.15 M. Following energy minimization and equilibration, production runs were conducted under NPT conditions (300 K, 1 atm) using the Nosé–Hoover thermostat and isotropic barostat. Trajectories were saved every 50 ps. Post-simulation analyses included RMSD, RMSF, Rg, SASA, MolSA, PSA, protein–ligand contacts using Desmond and Maestro. Simulated complexes were compared with the control to evaluate relative stability and binding behavior.

2.12.9 Post simulation MM-GBSA analysis

Binding free energies of ligand–protein complexes were estimated using the molecular mechanics generalized Born surface area (MM-GBSA) method [65], over 100 ns MD trajectories via the Maestro interface (Schrödinger Release 2020-3) with default parameters.

2.12.10 PCA and DCCM analysis

Principal component analysis (PCA) and dynamic cross-correlation matrix (DCCM) analyses were performed using custom-built BioPython scripts to evaluate conformational flexibility, structural transitions, and correlated residue motions. These analyses provide insights into binding behavior, complex stability, protein dynamics, and potential allosteric communication pathways [66].

2.12.11 Free energy landscape analysis

Stability of phytochemical–protein and control complexes were assessed using RMSD–Rg based free energy landscapes derived from MD trajectories to evaluate structural compactness, conformational stability, and energetically favorable states [67]. A custom-built Bio-Python script was used to compute the calculation.

2.12.12 Gibbs free energy analysis

Gibbs free energy landscapes were generated using a custom Python script based on Boltzmann statistics, mapping dominant conformational states via PC1 and PC2 [68, 69].

3. Results

3.1 Preliminary phytochemical screening

The preliminary phytochemical analysis of MEHFL revealed the presence of phenols, flavonoids, tannins, terpenoids, reducing sugars, anthraquinones, saponins, and steroids.

3.2 Quantitative determination of bioactive phytoconstituents (TPC, TFC, TTC)

The phenolic content of MEHFL was quantified using standard calibration curves. TPC was calculated from the regression equation $y = 5.88 \times 10^{-3} x + 0.15$ ($R^2 = 0.98$; Additional file 1, Figure SF1), yielding a result of 78.92 ± 0.26 mg GAE/g dry extract. TTC was calculated using the regression equation $y = 6.58 \times 10^{-3} x + 0.37$ ($R^2 = 0.95$; Additional file 1, Figure SF2), resulting in 245.92 ± 0.60 mg GAE/g dry extract. Both TPC and TTC were calculated using gallic acid as the standard. TFC was measured using $y = 0.36x - 0.02$ ($R^2 = 0.98$; Additional file 1, Figure SF3), giving 1.56 ± 0.06 mg QE/g dry extract, with quercetin as the reference standard.

3.3 In vitro antioxidant assays

3.3.1 DPPH free radical scavenging assay

The free radical scavenging activity of MEHFL increased in a concentration-dependent manner (Figure 1A). The DPPH assay revealed significantly greater ($p < 0.001$) antioxidant potency of MEHFL than the positive control, ascorbic acid, as reflected by lower IC_{50} values. MEHFL exhibited an IC_{50} of 21.98 ± 1.19 µg/mL, whereas ascorbic acid showed a higher IC_{50} of 59.58 ±

2.06 µg/mL, indicating lower activity. At 200 µg/mL, MEHFL achieved a maximum inhibition of 85.77 ± 0.04%, surpassing that of ascorbic acid (66.84 ± 0.13%) at the same concentration (Additional file 1, Table ST1).

3.3.2 Ferricyanide reducing power assay

The reducing power of MEHFL was found to increase with increasing concentration (Figure 1B). A strong linear relationship was observed for both MEHFL ($R^2 = 0.87$) and ascorbic acid ($R^2 = 0.86$). At all tested concentrations, MEHFL exhibited higher absorbance values than ascorbic acid (Additional file 1, Table ST2). At 400 µg/mL, MEHFL showed an absorbance of 1.29 ± 0.002 compared with 0.44 ± 0.001 for ascorbic acid, with the difference being statistically significant ($p < 0.001$).

3.4 In vitro anti-inflammatory assays

3.4.1 Bovine serum albumin (BSA) denaturation assay

MEHFL inhibited bovine serum albumin denaturation in a concentration-dependent manner (Figure 1C). At all concentrations tested, MEHFL exhibited significantly greater inhibition than aspirin (Additional file 1, Table ST3). Maximum inhibition by MEHFL was 91.35 ± 2.22% at 2000 µg/mL, compared with 77.77 ± 1.85% for aspirin. Consistent with this, IC_{50} analysis indicated significantly higher anti-inflammatory activity of MEHFL relative to the positive control ($p < 0.001$), with IC_{50} values of 966.61 ± 0.45 µg/mL for MEHFL and 1380.23 ± 0.95 µg/mL for aspirin.

3.4.2 Egg albumin denaturation assay

MEHFL also inhibited egg albumin denaturation in a concentration-dependent manner (Figure 1D), exceeding the activity of diclofenac at all concentrations (Additional file 1, Table ST4). Maximum inhibition by MEHFL was 78.78 ± 0.87%, higher than diclofenac (64.14 ± 1.33%). The IC_{50} of MEHFL (834.85 ± 0.52 µg/mL) was significantly lower than that of diclofenac (1300.75 ± 0.85 µg/mL; $p < 0.001$), indicating superior anti-inflammatory potency.

3.5 In vitro antidiabetic assays

3.5.1 α-Amylase inhibition assay

The α-amylase enzyme was inhibited by the MEHFL in a concentration-dependent manner (Figure 1E), with the percentage inhibition 90.32 ± 0.29% at 400 µg/mL surpassing acarbose (65.02 ± 0.29%) at the same concentration (Additional file 1, Table ST5). Consistently, MEHFL exhibited a significantly lower IC_{50} value (40.07 ± 0.18 µg/mL) than acarbose (78.52 ± 0.32 µg/mL; $p < 0.001$), indicating superior antidiabetic potential.

3.5.2 α-Glucosidase inhibition assay

MEHFL inhibited α-glucosidase in a concentration-dependent manner, similar to α-amylase (Figure 1F). At all concentrations, MEHFL demonstrated significantly greater inhibition than acarbose (Additional file 1, Table ST6). Maximum inhibition by MEHFL was 74.09 ± 0.92% at 400 µg/mL, compared with 67.21 ± 0.61% for acarbose. IC_{50} values confirmed significantly higher antidiabetic activity of MEHFL (35.75 ± 1.42 µg/mL) relative to acarbose (84.34 ± 2.01 µg/mL; $p < 0.001$).

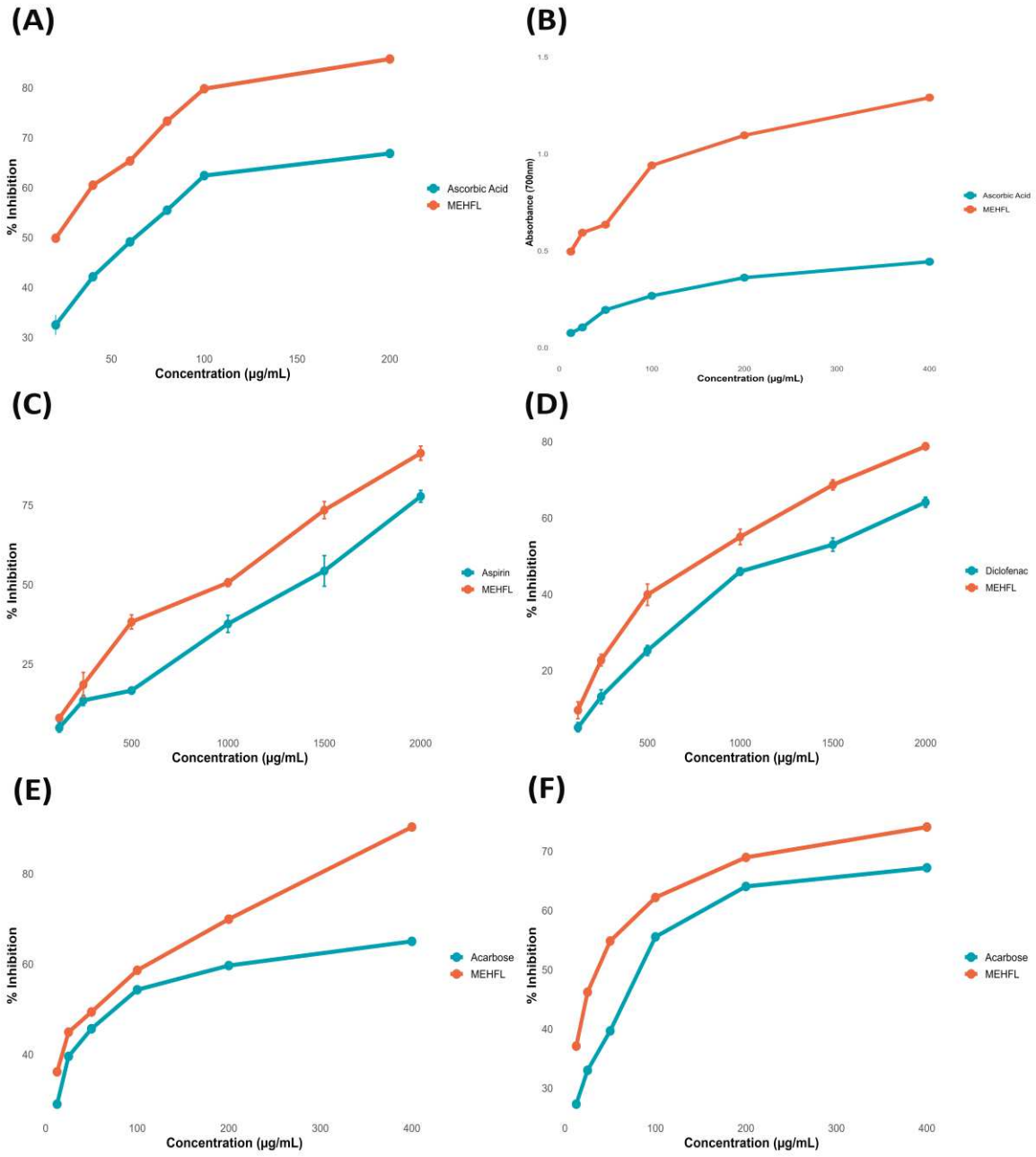


Figure 1: Concentration–response profiles of the methanolic extract of *H. fomes* leaves (MEHFL) across in vitro assays compared with respective positive controls: (A) DPPH free radical scavenging, (B) ferricyanide reducing power, (C) BSA denaturation, (D) egg albumin denaturation, (E) α-amylase inhibition, and (F) α-glucosidase inhibition. Data are represented as mean ± SEM, n = 3.

3.6 Toxicological assessment

3.6.1 Brine shrimp lethality bioassay

MEHFL induced concentration-dependent mortality in brine shrimp nauplii over the range of 12.5–400 µg/mL (Figure 2A). Mortality rates for MEHFL ranged from 4.44 ± 2.22% to 55.56 ± 2.22%, whereas the control produced 24.44 ± 2.22% to 77.78 ± 5.88% mortality (Additional file 1, Table ST7). The LC_{50} value of MEHFL (328.57 ± 2.12 µg/mL) was significantly higher than that of the control (56.25 ± 4.62 µg/mL), indicating moderate toxicity of MEHFL ($LC_{50} \leq 500$ µg/mL) and high toxicity of the control ($LC_{50} < 100$ µg/mL) according to Meyer's toxicity index [70].

3.6.2 Acute oral toxicity study in mice model

The 14-day trial showed no mortality in the study animals treated with MEHFL, indicating that the LD_{50} of MEHFL exceeds 5000 mg/kg. However, hyperactivity was observed in the mice for some hours on the first day following MEHFL administration, which normalized in the subsequent days of the trial (Additional file 1, Table ST8). Apart from this, no changes in behavioral patterns, physical appearance, or signs of illness were noted during the 14-day trial period. Though, body weight gradually increased in both groups (Figure 2A), statistical analysis did not reveal any significant difference between the MEHFL and control group (Additional file 1, Table ST9).

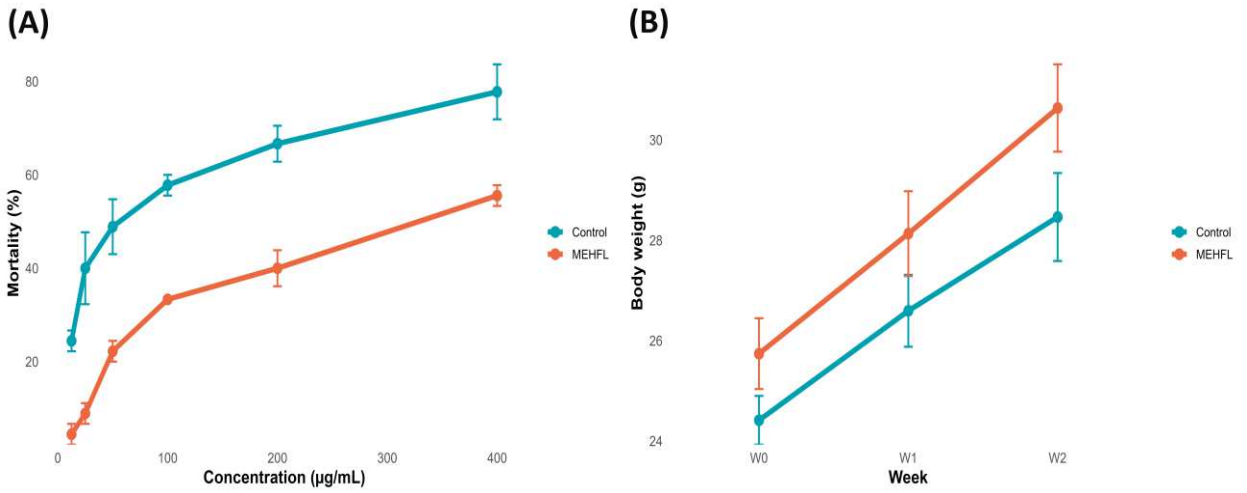


Figure 2: Toxicological assessment of the methanolic extract of *H. fomes* leaves (MEHFL). (A) Dose–response relationship between MEHFL and the control, illustrating percentage mortality of brine shrimp nauplii (n = 3). Data are expressed as mean ± SEM (n = 3). (B) Body weight changes of mice during the acute oral toxicity study of MEHFL, recorded on day 0 (W0), day 7 (W1), and day 14 (W2). Data are presented as mean ± SEM (n = 5), with statistical comparisons performed using Welch's *t*-test.

3.7 In vivo antidiabetic assays

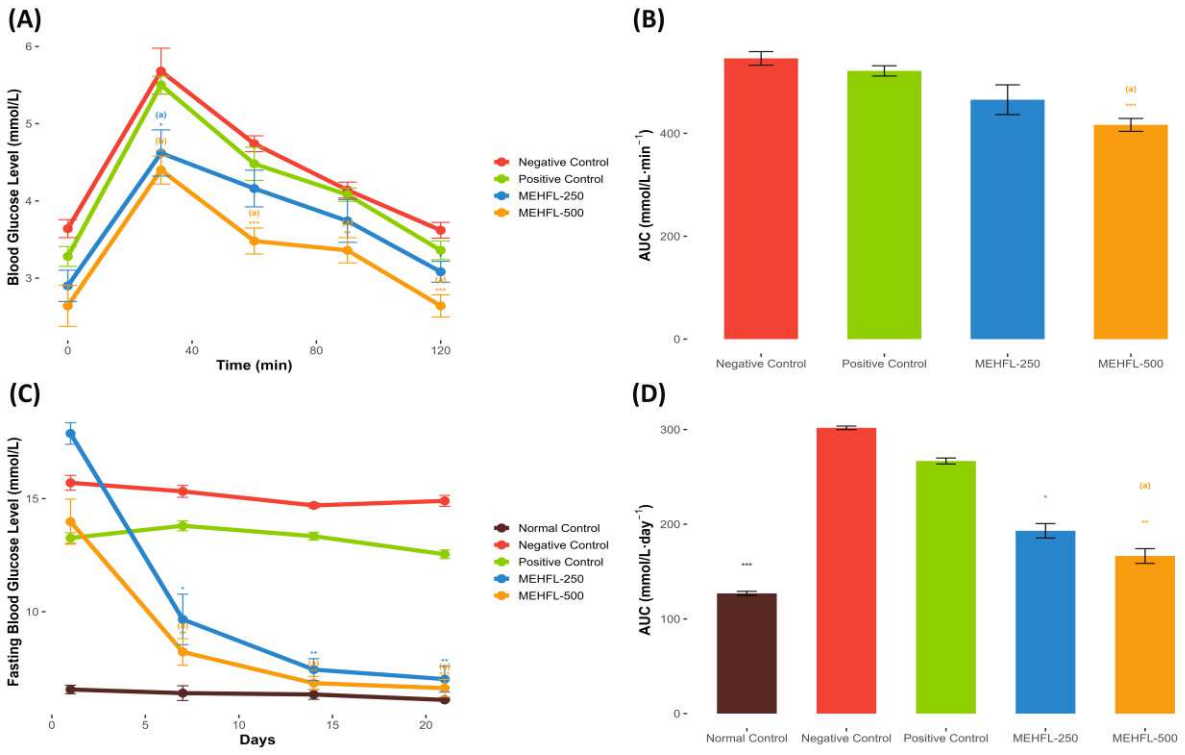
3.7.1 Oral glucose tolerance test (OGTT) in non-diabetic mice

Both doses of MEHFL significantly attenuated the peak blood glucose level at 30 min compared with both control groups (Figure 3A). MEHFL-250 produced a significant reduction ($p < 0.05$), whereas MEHFL-500 elicited a more pronounced effect ($p < 0.01$) (Additional file 1, Table ST10). Overall glycemic response was evaluated using the area under the curve (AUC) (Figure 3B; Additional file 1, Table ST10). Although MEHFL-250 reduced the AUC (465.33 ± 28.93 mmol/L·min^{-1}), this reduction was not statistically significant relative to the negative (545.70 ± 13.21 mmol/L·min^{-1}) and positive (521.40 ± 9.97 mmol/L·min^{-1}) control groups. In contrast,

MEHFL-500 significantly decreased the AUC (416.40 ± 12.52 mmol/L·min^{-1}) compared with both controls. MEHFL-500 also exhibited the lowest total blood glucose level over the study period (13.88 ± 0.38 mmol/L) among all experimental groups (Additional file 1, Table ST10).

3.7.2 Assessment of fasting blood glucose (FBG) level in alloxan-induced diabetic rats

Weekly monitoring of FBG over the 21-day treatment period revealed a marked reduction in FBG levels following MEHFL administration compared with the negative control (Figure 3C). However, only the higher dose (MEHFL-500) produced significantly lower FBG levels than the positive control at all time points. Area under the curve (AUC) analysis further reflected the cumulative glycemic burden during the study (Figure 3D). MEHFL-250 significantly reduced the AUC compared with the negative control only, whereas MEHFL-500 resulted in a significant decrease in AUC relative to both control groups. The normal control group exhibited the lowest AUC, whereas the negative control group showed the highest value (127.01 ± 2.12 and 301.73 ± 1.90 mmol/L·day^{-1} for the normal and negative control groups, respectively; Additional file 1, Table ST11). Untreated diabetic rats maintained the highest blood glucose levels throughout the study (day 1–21), with a cumulative glucose level of 60.62 ± 0.41 mmol/L, while the normal control consistently showed the lowest levels (25.40 ± 0.37 mmol/L; Additional file 1, Table ST11). Both MEHFL doses significantly reduced total blood glucose levels compared with the negative control; however, only MEHFL-500 achieved a significantly lower glucose level (35.66 ± 1.81 mmol/L) than the positive control (52.94 ± 0.54 mmol/L; $p < 0.05$).



479

480 **Figure 3:** Effect of the methanolic leaf extract of *H. fomes* (MEHFL) on blood glucose regulation
481 in in vivo antidiabetic models. Time-course profiles for the oral glucose tolerance test (OGTT) and
482 alloxan-induced diabetes models are shown in (A) and (C), respectively, with corresponding areas
483 under the curve (AUC) presented in (B) and (D). Statistical significance is denoted by *, **, and
484 *** ($p < 0.05$, 0.01, and 0.001, respectively) versus the negative control, and by (a), (b), and (c) (p
485 < 0.05, 0.01, and 0.001, respectively) versus the positive control (one-way ANOVA followed by
486 Dunnett's post hoc test). Data are expressed as mean ± SEM (n = 5).

487 **3.8 Characterization and identification of phytoconstituents**

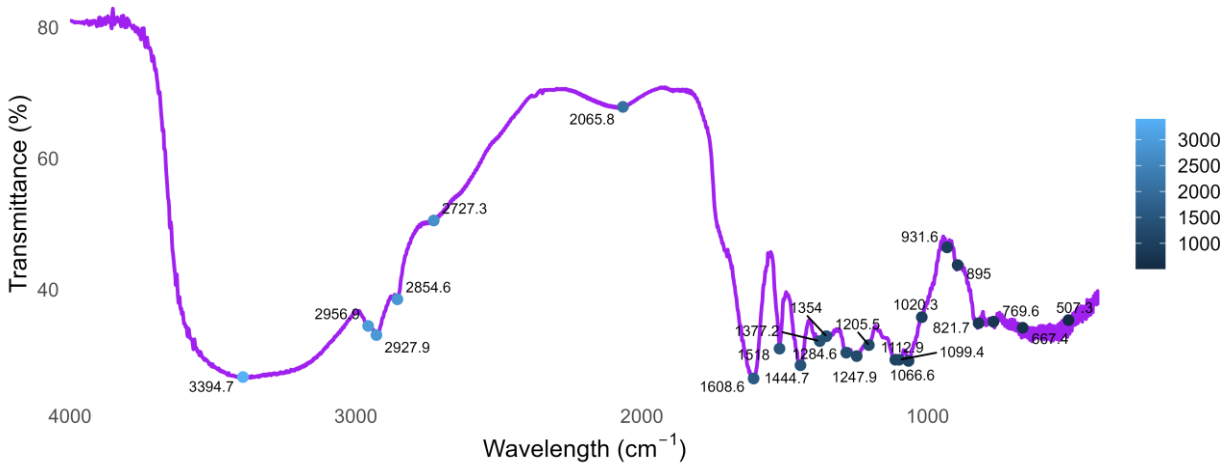
488 **3.8.1 Fourier-Transform Infrared (FTIR) spectroscopy analysis**

489 Functional groups present in MEHFL (Table 2) were identified through interpretation of the FTIR
490 spectra (Figure 4). The analysis confirmed the presence of diverse chemical functionalities.
491 Notably, a broad O–H stretching band, together with prominent aromatic C=C vibrations and

characteristic out-of-plane C–H bending, indicates a phenolic-rich extract. In addition, intense C–O–C and C–O stretching bands in the 1200–1000 cm^{-1} region suggest sugar conjugates, while CH_2/CH_3 stretching and alkene bending vibrations imply the presence of fatty acids, terpenes, or sterol-like compounds.

Table 2: FTIR spectral peak assignments of the methanolic extract of *H. fomes* leaves (MEHFL).

Characteristic Absorption (cm^{-1})	Bond	Functional Group
3394.7	O–H stretch, H-bonded	Alcohols, Phenols
2956.9	C–H stretch (asymmetric)	Alkanes (CH_3)
2927.9	C–H stretch (asymmetric)	Alkanes (CH_2)
2854.6	C–H stretch (symmetric)	Alkanes (CH_2)
2727.3	C–H stretch (aldehyde)	Aldehydes (–CHO)
2065.8	C≡C stretch	Alkynes
1608.6	C=C stretch (aromatic)	Aromatic ring
1518.0	C=C stretch (aromatic)	Aromatic ring
1444.7	C–H bending (CH_2)	Alkanes
1377.2	C–H bending (CH_3)	Alkanes
1354	C–H wag	Alkyl halides / C–O stretch
1284.6	C–O stretch	Esters, Ethers
1247.9	C–O stretch	Esters, Ethers
1205.5	C–O stretch	Alcohols, Ethers
1112.9	C–O–C stretch	Ether linkage
1099.4	C–O stretch	Alcohols, Esters
1066.6	C–O stretch	Primary alcohols
1020.3	C–O–C stretch	Ether linkage
931.6	=C–H out-of-plane bend	Alkenes (trans)
895	=C–H out-of-plane bend	Alkenes (vinylidene)
821.7	C–H out-of-plane bend	Aromatic (1,4-disubstituted)
769.6	C–H out-of-plane bend	Aromatic (mono/substituted)
667.4	C–H wag	Alkyl halides (C–Cl)
507.3	C–C stretch / C–X stretch	Alkyl halides



498

499 **Figure 4:** FTIR spectra of the methanolic extract of *H. fomes* leaves (MEHFL).

500 **3.8.2 Gas Chromatography–Mass Spectrometry (GC–MS) profiling**

501 GC–MS analysis of MEHFL revealed the presence of 97 distinct phytochemicals spanning a broad
502 range of chemical classes (Figure 5). The relative abundance of these constituents suggests their
503 potential contribution to the biological activities of the extract. The most abundant compound was
504 rhodopin, with a retention time of 36.72 min (Additional file 1, Table ST12). The second and third
505 most abundant compounds were identified as (E,E,E)-3,7,11,15-tetramethylhexadeca-1,3,6,10,14-
506 pentaene (36.37 min) and squalene (36.06 min), respectively.

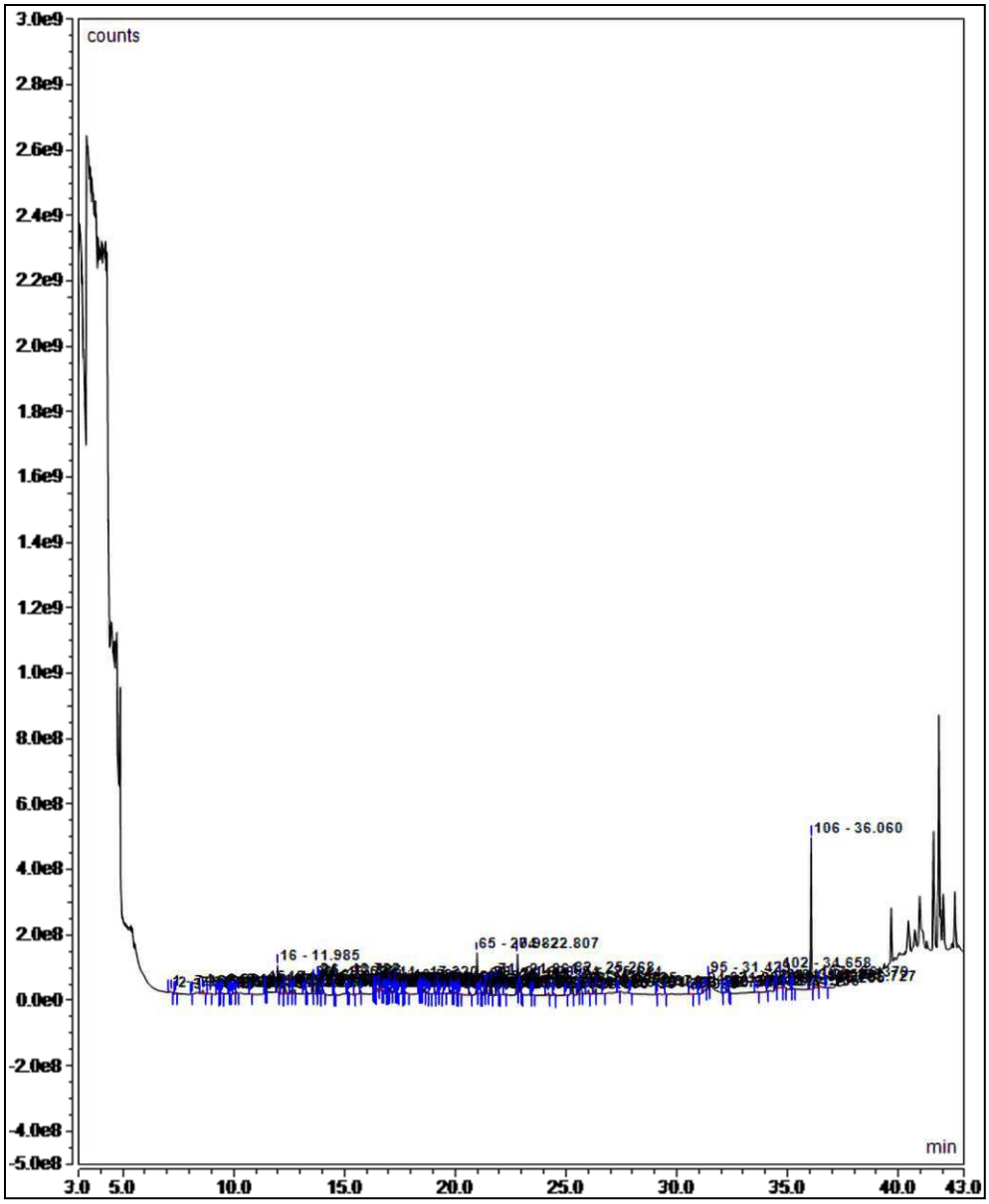


Figure 5: GC–MS chromatogram of the methanolic extract of *H. fomes* leaves (MEHFL).

3.9 In silico analysis

3.9.1 Ligand geometry optimization

To obtain reliable molecular geometries of GC–MS-guided phytochemicals from MEHFL, density functional theory (DFT) calculations were performed at the B3LYP/6-311G(d,p) level using the

Gaussian 09 software package (Additional file 2, Table ST13). The optimized structures are depicted with atom-specific labels and symbols, and distinct color codes are used to represent different atomic species within the molecules (Figure 6).

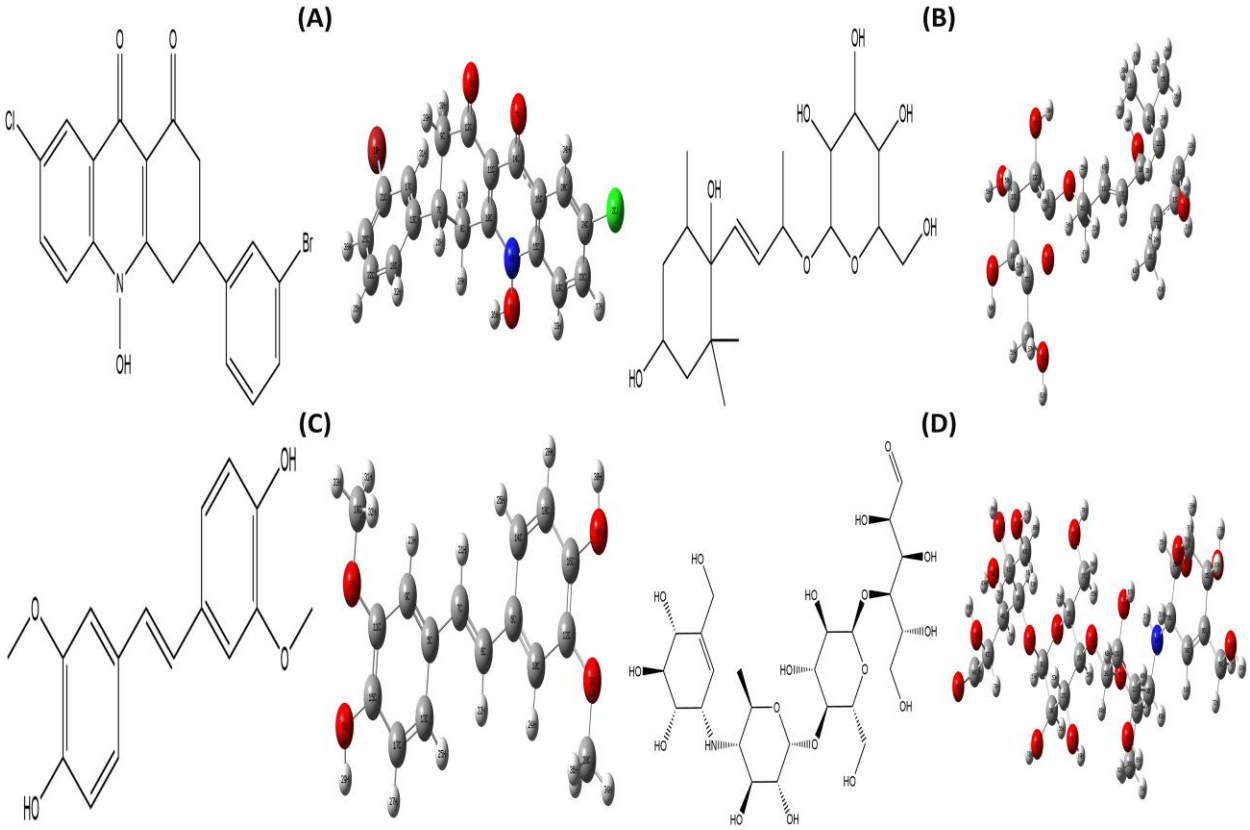


Figure 6: Two- and three-dimensional representations of some geometry-optimized compounds derived from the methanolic extract of *H. fomes* leaves (MEHFL): (A) Compound 61, (B) Compound 78, and (C) Compound 88. The control compound, acarbose, is shown in (D). In each illustration, the left side depicts the two-dimensional chemical structure, while the right side illustrates the corresponding three-dimensional optimized conformation.

3.9.2 Structure validation and active site prediction of the target proteins

The structural quality of the selected crystal protein structures was evaluated using multiple validation tools (Table 3). Both proteins exhibited acceptable quality based on ERRAT and

VERIFY3D scores. PROCHECK Ramachandran plots (Additional file 2, Figure SF4) showed favorable backbone conformations, with no disallowed residues in 2QV4 and two in 3A4A. ProSA-web z-scores were within the range of experimentally determined NMR structures, and residue-wise energy profiles showed minimal anomalies (Additional file 2, Figure SF5), confirming structural suitability for computational studies. Binding-site prediction using PrankWeb identified two and five pockets in 2QV4 and 3A4A, respectively, with pocket 1 selected for docking analysis (Additional file 2, Table ST14 and SF3).

Table 3: Validation metrics of the selected protein structures for computational analysis.

Protein Name	PDB ID	ERRAT	VERIFY 3D	PROCHECK Ramachandran plot			ProSA Z score
				Residues in most favored region	Residues in additional allowed region	Residues in disallowed regions	
α amylase	2QV4	Overall quality factor: 95.8763	Pass 91.31% of the residues have averaged 3D-1D score >= 0.1	361 (86.0%)	57 (13.6%)	0 (0.0%)	−9.56
α glucosidase	3A4A	Overall quality factor: 93.2526	Pass 99.15% of the residues have averaged 3D-1D score >= 0.1	461 (88.5%)	58 (11.1%)	2 (0.4%)	−10.43

Data were obtained using SAVES v6.1 (ERRAT, VERIFY3D, and PROCHECK) and ProSA-Web.

3.9.3 Molecular docking analysis

Following molecular docking of GC–MS-identified MEHFL-derived compounds against α-amylase and α glucosidase, candidates with docking scores equal to or more negative than the control were shortlisted (Additional file 2, Table ST15). Nine compounds for α-amylase and seven for α-glucosidase met this criterion. Among these, compound 17 and 61 showed the highest and

second-highest affinities against both targets, respectively. Compound 17 exhibited binding affinities of −10.4 and −10.5 kcal/mol toward α-amylase and α glucosidase, respectively, whereas compound 61 showed affinities of −9.9 and −9.4 kcal/mol. Subsequent molecular interaction profiling was conducted to prioritize ligands based on the number of direct hydrogen bonds formed with active-site residues. Compounds forming multiple hydrogen bonds were preferentially selected. Accordingly, compounds 17, 30, 61, 88, and 94 were shortlisted against α amylase, while compounds 17, 61, 78, and 94 were selected against α-glucosidase (Additional file 2, Table ST15). Among these, compound 17 formed the highest number of hydrogen bonds with both targets. In α amylase, compound 17 formed six hydrogen bonds with ALA106 (2.80 Å), HIS299 (2.43 Å), ASP300 (2.37, 2.52 Å), ASP197 (2.39 Å), and HIS305 (3.54 Å). Similarly, in α glucosidase, it formed six hydrogen bonds with THR310 (2.70 Å), ASP242 (2.05, 3.51 Å), TYR158 (2.37 Å), PRO312 (2.99 Å), and GLU411 (2.67 Å) (Additional file 2, Table ST16). Compound 78 showed the second-highest number of hydrogen bonds against α glucosidase, interacting with ARG315 (5.16 Å), GLN353 (2.05 Å), LEU313 (1.88 Å), and TYR158 (2.60 Å) (Figure 7). The remaining selected compounds formed two hydrogen bonds at the active sites of both enzymes. Notably, although the control ligand exhibited lower docking scores, it formed a more extensive interaction network with both targets (Figure 7).

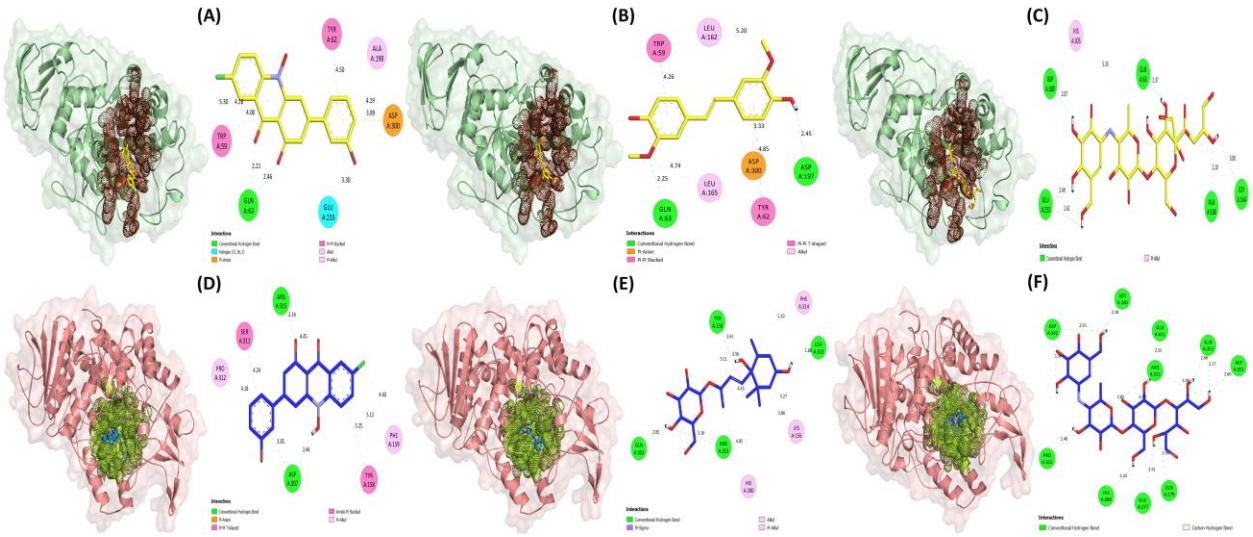


Figure 7: Molecular interaction profiles of some shortlisted GC–MS-guided compounds from the methanolic extract of *H. fomes* leaves (MEHFL) with α-amylase and α glucosidase. The upper panel depicts interactions of (A) compound 61, (B) compound 88, and (C) the control with α-amylase at the predicted active site (brown dotted region). The lower panel shows interactions of (D) compound 61, (E) compound 78, and (F) the control with α-glucosidase at the predicted active site (green dotted region). For each illustration, three-dimensional interaction views are shown on the left, with corresponding two-dimensional interaction maps on the right.

3.9.4 Physicochemical properties, drug likeliness and ADMET prediction

All shortlisted compounds largely conformed to Lipinski's rule of five, with the exception of compound 17, while compound 78 exhibited a single violation attributable to an elevated hydrogen-bond donor count (Table 4). Compounds 30, 88, and 94 demonstrated an optimal balance between lipophilicity and aqueous solubility, whereas compounds 17 and 61 were predicted to be more lipophilic and the control compound highly hydrophilic. Predicted bioavailability scores supported favorable oral exposure for all shortlisted compounds except compound 17. None of the candidates showed structural alerts for assay interference, and all were

predicted to be synthetically more accessible than the control. Comprehensive ADMET profiling indicated superior intestinal absorption for all shortlisted compounds relative to the control (Figure 8 and Additional file 2, Table ST17). Compounds 30, 61, and 88 exhibited ≥30% predicted human oral bioavailability, whereas compounds 17 (<20%), 78, and 94 (<30%) showed comparatively lower values. P-glycoprotein interactions were predicted for compounds 17, 61, and 94. Except for compound 78, all candidates displayed higher steady-state volumes of distribution than the control, suggesting enhanced tissue penetration; notably, compound 94 showed distribution parameters within optimal ranges. Cytochrome P450 liabilities were minimal for compound 78 but most pronounced for compound 61, while only compound 17 was predicted to inhibit OATP1B1. All shortlisted compounds were predicted to undergo faster clearance than the control, with longer elimination half-lives except for compound 88. In silico toxicity assessment identified potential hepatotoxicity for compounds 17 and 30 and the control, mutagenicity for compound 17, and a low predicted LD_{50} for compound 94.

Table 4: Physicochemical properties, drug-likeness, and medicinal chemistry profiles of GC–MS-identified shortlisted compounds from the methanolic extract of *H. fomes* leaves (MEHFL).

General information			Physicochemical properties									Drug likeliness		Medicinal chemistry	
Compound Number	Name	PubChem CID	MW (g/mol)	NHA	NAHA	NRB	NHBA	NHBD	Log $P_{o/w}$	Log S	Solubility	Lipinski	Bioavailability score	PAINS	Synthetic accessibility
17	5-(3-acetyl-1-(2-((2S,4R)-2-((6-bromopyridin-2-yl)carbamoyl)-4-fluoropyrrolidin-1-yl)-2-oxoethyl)-1H-indazol-5-yl)-2-aminopyrimidine 1-oxide	126623006	597.40	39	21	8	9	3	1.72	-4.53	Moderate	No; 2 Violations	0.17	0 alert	4.58
30	1,3-Bis(3-methylphenyl)urea	136428	240.30	18	12	4	1	2	3.19	-3.72	Soluble	Yes; 0 Violations	0.55	0 alert	1.79
61	3-[3-Bromophenyl]-7-chloro-3,4-dihydro-10-hydroxy-1,9(2H,10H)-acridinedione	536420	418.67	25	16	1	3	1	3.71	-4.90	Moderate	Yes; 0 Violations	0.55	0 alert	3.45
78	(3S,5R,6S,7E,9x)-7-Megastigmene-3,6,9-triol 9-glucoside	16745401	390.47	27	0	5	8	6	0.03	-1.73	Very Soluble	Yes; 1 Violations	0.55	0 alert	6.12
88	(E)-4,4'-(ethene-1,2-diyl)bis(2-methoxyphenol)	5280698	272.30	20	12	4	4	2	3.06	-4.18	Moderately soluble	Yes; 0 Violations	0.55	0 alert	2.24
94	(5ß)Pregnane-3,20ß-diol, 14a,18a-[4-methyl-3-oxo-(1-oxa-4-azabutane-1,4-diyl)]-, diacetate	N/A	419.55	30	0	7	6	1	3.10	-4.23	Moderately soluble	Yes; 0 Violations	0.55	0 alert	4.83
Control	Acarbose	9811704	645.60	44	0	13	19	14	-6.24	2.57	Highly soluble	No; 3 Violations	0.17	0 alert	7.25

Abbreviations: MW = Molecular weight, NHA = Number of heavy atoms, NAHA = Number of aromatic heavy atoms, NRB = Number of rotatable bonds, NHBA = Number of hydrogen bond acceptor, NHBD = Number of hydrogen bond donor and TPSA = Topological polar surface area.

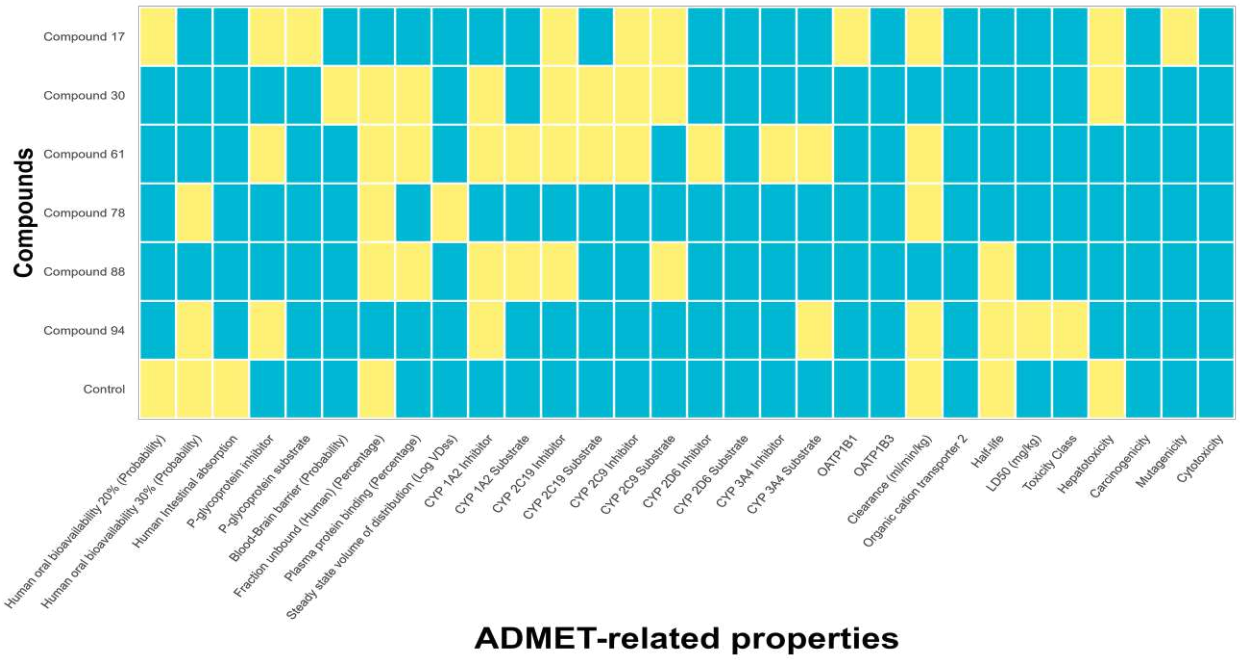
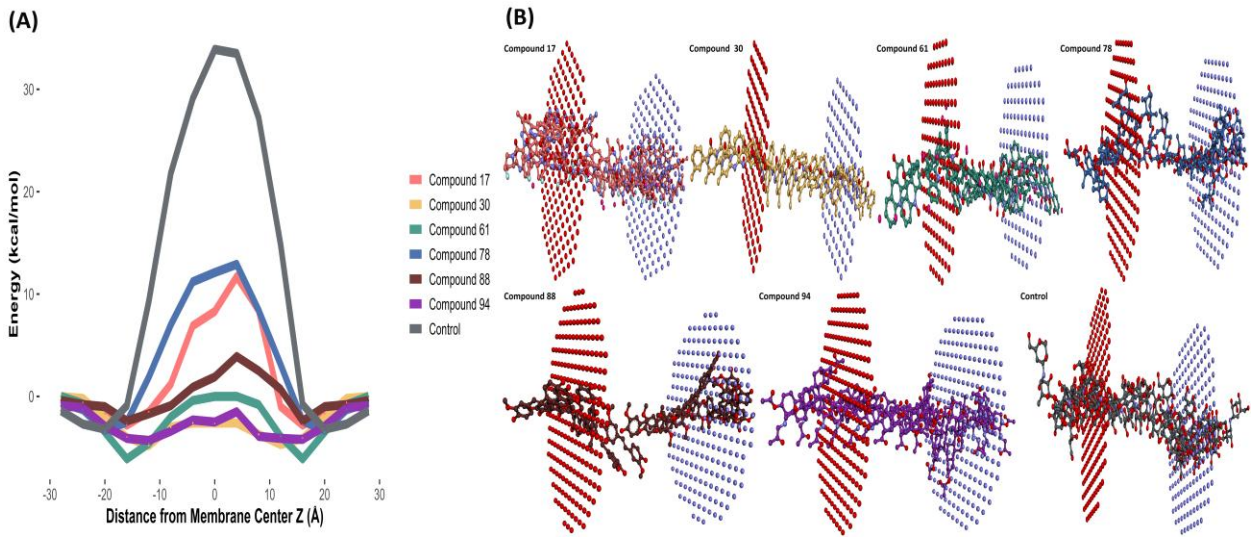


Figure 8: Heat map of ADMET profiles of shortlisted GC–MS-identified compounds from the methanolic extract of *H. fomes* leaves (MEHFL). Blue indicates values within acceptable ranges, whereas yellow denotes deviations. For enzyme-related parameters, yellow indicates predicted interaction (substrate and/or inhibitor) and blue indicates non-interaction. For toxicity endpoints, blue denotes inactive and yellow denotes active predictions. Assessed through SwissADME, ADMETLab 2.0, Deep-PK and ProTox 3.0 web tools.

3.9.5 Passive permeability assessment

Membrane permeability analysis indicated that shortlisted compounds traversed the phospholipid bilayer with lower energetic penalties than the control, reflecting enhanced passive diffusion (Figure 9A). Compounds 30 and 94 showed the most favorable central bilayer energetics, while compound 61 exhibited neutral energy at the membrane midpoint and a binding free energy of −6.19 kcal/mol (Additional file 2, Table ST18). Trajectory analysis demonstrated adaptive membrane alignment and greater insertion stability relative to the control (Figure 9B).



612

613 **Figure 9:** Predicted passive plasma membrane permeability of shortlisted GC–MS-identified
614 compounds from the methanolic extract of *H. fomes* leaves (MEHFL). (A) Energy transfer profiles
615 across the phospholipid bilayer. (B) Spatial localization and optimized orientations of the
616 compounds within the plasma membrane, obtained using PerMM server.

617 **3.9.6 Compound selection**

618 The shortlisted compounds demonstrated superior binding affinities toward both targets relative to
619 the control, with comparable interaction profiles and overall favorable pharmacological
620 characteristics. Compounds 17 and 30 were excluded due to predicted toxicity risks. Although
621 compound 94 exhibited promising ADME and membrane permeability properties, its low
622 predicted LD_{50} suggested a potentially narrow therapeutic index [71, 72]. Consequently,
623 compounds 61, 78, and 88 were advanced based on robust docking performance, favorable ADME
624 attributes, absence of predicted toxicity, and enhanced passive membrane permeability.

625 **3.9.7 Off-target effects prediction**

In silico off-target profiling was conducted to identify the most probable alternative targets of the selected compounds beyond α-amylase and α-glucosidase (Figure 10; Additional file 2, Table ST19), providing additional insight into potential off-target interactions and pharmacological versatility. Compound 61 was predominantly predicted as a protease inhibitor, with matrix metalloproteinases comprising the majority of its top-ranked targets. Compounds 78 and 88 exhibited broader target diversity across multiple protein classes. Notably, the top predicted targets of compound 78 included sodium/glucose cotransporters 1 and 2, whereas compound 88 showed prominent associations with the NF-κB p65 subunit and cyclooxygenase-2. These predictions suggest potential therapeutic relevance in mitigating T2DM associated oxidative stress and inflammation [73–77].

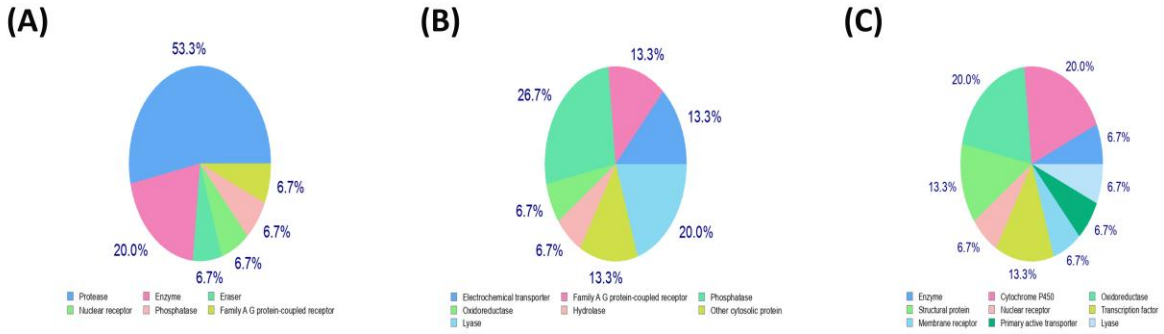


Figure 10: Predicted off-target profiles of the selected GC–MS identified compounds from the methanolic extract of *H. fomes* leaves (MEHFL), using SwissTargetPrediction web tool. (A) Compound 61, (B) Compound 78, and (C) Compound 88.

3.9.8 Quantum chemical reactivity analysis

3.9.8.1 Frontier molecular orbital analysis

HOMO–LUMO analysis elucidated the electronic distribution and reactivity of the selected compounds (Table 5; Figure 11). Compounds 61 and 88 exhibited smaller HOMO–LUMO gaps

than the control, indicating enhanced chemical reactivity due to facilitated electronic transitions [78]. In contrast, compound 78 showed a larger gap, suggesting greater chemical stability relative to the control. All screened compounds displayed less negative HOMO energies than the control, reflecting increased electron-donating ability and reactivity; however, such features may confer higher susceptibility to oxidative metabolic transformations [79].

Table 5: Comprehensive DFT-derived quantum chemical parameters of selected GC–MS-identified compounds from the methanolic extract of *H. fomes* leaves (MEHFL).

Compound	E_{HOMO}	E_{LUMO}	E_{gap}	I	A	χ	μ	η	σ	ω
Hit61	−9.46	−1.29	8.17	1.29	9.46	5.37	−5.37	−4.08	−0.24	−3.54
Hit78	−9.89	0.47	10.36	−0.47	9.89	4.70	−4.70	−5.18	−0.19	−2.13
Hit88	−8.35	−0.37	7.97	0.37	8.35	4.36	−4.36	−3.98	−0.25	−2.38
Control	−10.02	−0.518	9.50	0.51	10.02	5.26	−5.26	−4.75	−0.21	−2.92

E_{gap} = energy gap (eV); E_{LUMO} = lowest unoccupied molecular orbital (eV); E_{HOMO} = highest occupied molecular orbital (eV); I = ionization potential (eV); A = electron affinity (eV); μ = chemical potential (eV); χ = electronegativity (eV); ω = electrophilicity index (eV); η = chemical hardness (eV); and σ = chemical softness (eV^{-1}).

3.9.8.2 Molecular electrostatic potential (MEP) analysis

Molecular electrostatic potential (MEP) mapping delineated electrophilic and nucleophilic reactive regions and hydrogen-bonding propensity (Figure 11). Oxygen atoms exhibited the most negative potentials, whereas hydrogen atoms showed the highest positive potentials. Electrostatic values ranged from +6.87 to +8.68 a.u. and −6.87 to −8.68 a.u.; the control spanned ±8.68 a.u. Compound 88 displayed the lowest absolute potential values, indicating a more evenly distributed charge profile.

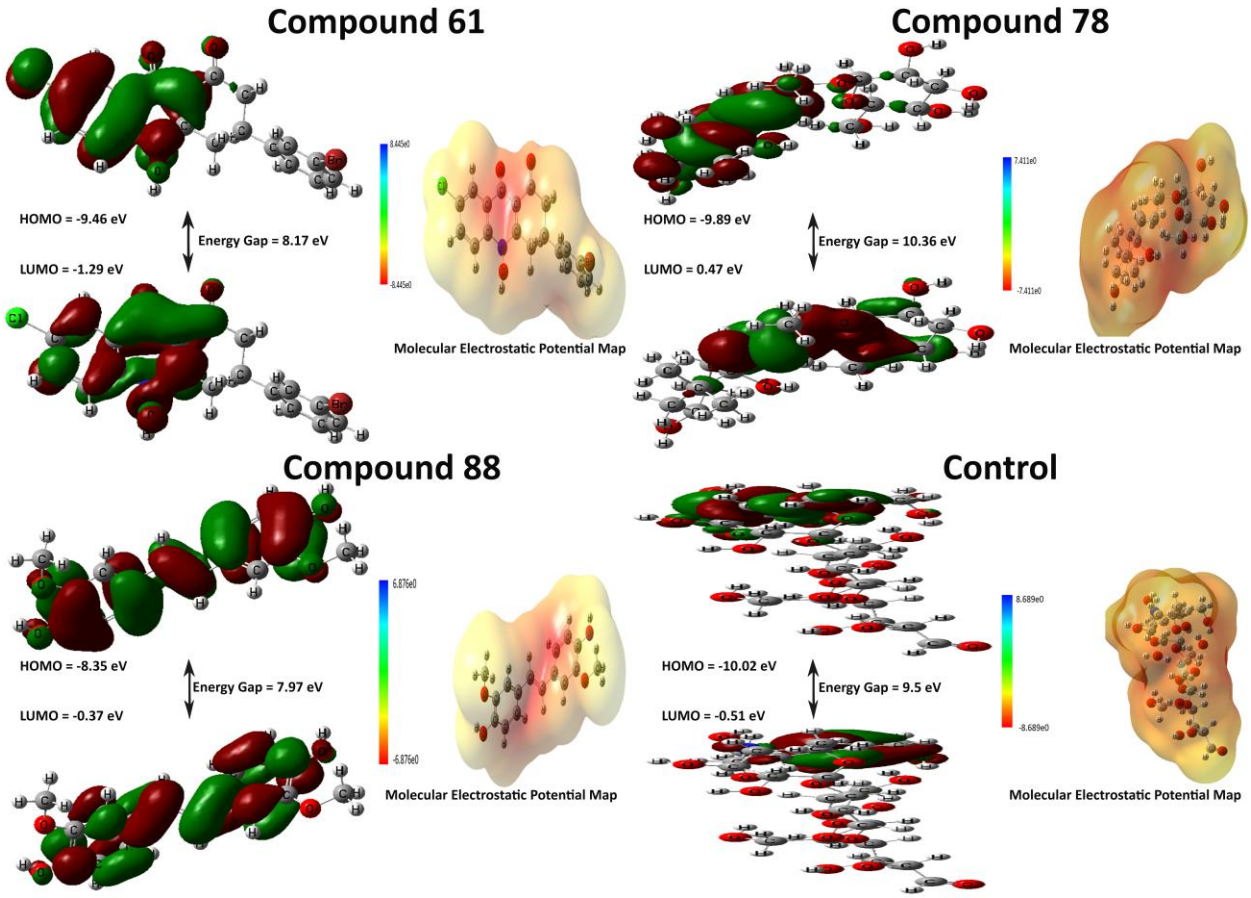


Figure 11: Frontier molecular orbitals (FMO) and molecular electrostatic potential (MEP) maps of optimized geometries of selected GC–MS identified compounds from the methanolic extract of *H. fomes* leaves (MEHFL).

3.9.9 Molecular dynamics (MD) simulation

3.9.9.1 Root Mean Square Deviation (RMSD) analysis

The structural stability and conformational dynamics of protein–ligand complexes were evaluated over 100 ns MD simulations using Cα RMSD analysis (Figure 12A and B). In α amylase, the control exhibited lower Cα RMSD and minimal fluctuations (mean = 1.48 ± 0.12 Å), comparable to the apo form (mean = 1.47 ± 0.23 Å), whereas compound 88 maintained a consistently higher plateau (mean = 1.58 ± 0.13 Å). Compound 61 initiated near 1.0 Å and equilibrated at ~20–30 ns,

673 followed by a transient deviation between 40–60 ns, suggesting temporary conformational
674 rearrangement before partial stabilization (mean = 1.55 ± 0.19 Å). In α glucosidase, all complexes
675 attained Cα RMSD equilibrium within 15–30 ns. Consistent with α amylase, the control remained
676 the most compact throughout the simulation (mean = 1.28 ± 0.10 Å) and exhibited lower RMSD
677 fluctuations than the apo structure (mean = 1.50 ± 0.15 Å) after equilibration. In contrast,
678 compounds 61 and 78 displayed elevated plateau levels, with compound 61 showing moderate
679 deviation (mean = 1.60 ± 0.22 Å) and compound 78 exhibiting the highest and most sustained drift
680 (mean = 1.82 ± 0.35 Å), indicative of greater structural perturbation. Nevertheless, all systems
681 stabilized within 30 ns, and subsequent fluctuations likely reflect intrinsic protein flexibility rather
682 than instability, as overall RMSD values remained within acceptable limits (<3.0 Å), supporting
683 conformational stability [80].

684 Ligand RMSD profiles were assessed to determine binding stability, where lower values indicate
685 stable conformations and higher fluctuations suggest reduced stability [81] (Figure 12C and D).
686 Compound 61 exhibited the lowest mean ligand RMSD in both α-amylase (0.73 ± 0.27 Å) and α-
687 glucosidase (0.67 ± 0.44 Å), indicating stable binding. In α amylase, the control showed the highest
688 values (mean = 1.94 ± 0.23 Å), with compound 88 displaying intermediate mobility (mean = 1.22
689 ± 0.37 Å). In α glucosidase, compound 78 exhibited the highest ligand RMSD (mean = 1.96 ± 0.20
690 Å), while the control showed intermediate stability (1.78 ± 0.15 Å).

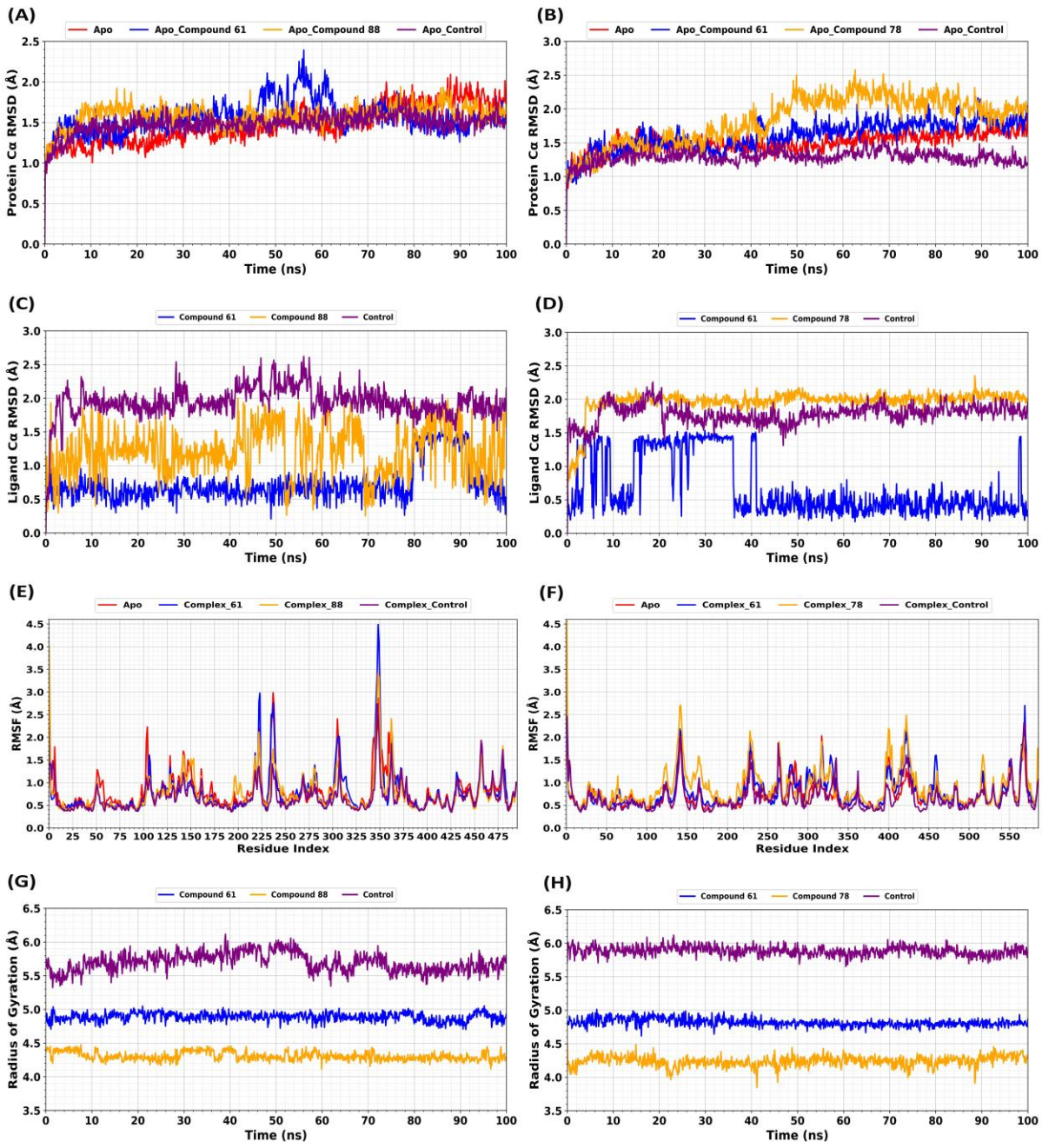
691 **3.9.9.2 Root Mean Square Fluctuation (RMSF) analysis**

692 Residue-level flexibility of the protein–ligand complexes was evaluated by RMSF analysis (Figure
693 12E and F). In both targets, the control exhibited the lowest mean RMSF values (0.67 ± 0.29 Å for
694 α amylase; 0.67 ± 0.56 Å for α glucosidase). In α amylase, compounds 61 (mean = 0.77 ± 0.48 Å)
695 and 88 (mean = 0.75 ± 0.41 Å) showed reduced overall flexibility relative to the apo structure

(mean = 0.82 ± 0.41 Å), although localized fluctuations (>3 Å) were observed at GLN349, ASN350, GLY351, and ASN352 for compound 61, and TYR2, ASN350, and GLY351 for compound 88. In α glucosidase, compound 61 (mean = 0.79 ± 0.66 Å) and compound 78 (mean = 0.90 ± 0.76 Å) showed higher fluctuation than apo form (mean = 0.73 ± 0.64 Å), with notable deviations at SER4 and SER5. Importantly, none of these highly fluctuating residues were located within the predicted active sites, supporting stable ligand binding [82].

3.9.9.3 Radius of gyration (Rg) analysis

Tertiary structural compactness was quantitatively assessed using Rg analysis, reflecting folding dynamics upon ligand binding (Figure 12G and H). Lower Rg values indicate increased compactness and structural stability, whereas higher values reflect reduced compactness and greater conformational entropy [80]. In α amylase, compounds 61 (4.88 ± 0.06 Å) and 88 (4.30 ± 0.06 Å) exhibited lower mean Rg values than the control (5.69 ± 0.13 Å). Similarly, in α glucosidase, compounds 61 (mean = 4.81 ± 0.05 Å) and 78 (mean = 4.23 ± 0.07 Å) showed greater compactness than the control (mean = 5.88 ± 0.06 Å). Collectively, these findings indicate enhanced structural stability of both targets upon binding of the selected *H. fomes*-derived ligands relative to the control.



712

713 **Figure 12:** Molecular dynamics simulation trajectories of selected GC–MS identified compounds
714 from the methanolic extract of *H. fomes* leaves (MEHFL) with α-amylase and α glucosidase. (A,
715 B) Cα RMSD; (C, D) ligand RMSD; (E, F) residue-wise RMSF; (G, H) radius of gyration (Rg)
716 for α-amylase and α glucosidase, respectively.

3.9.9.4 Solvent accessible, molecular and polar surface area assessment

SASA analysis was performed to evaluate protein surface exposure and structural adaptation upon ligand binding, where reduced SASA reflects tighter packing and enhanced stability [62]. In α-amylase (Figure 13A), compounds 61 (210.95 ± 30.94 Å²) and 88 (218.17 ± 42.35 Å²) exhibited lower mean SASA values than the control (260.16 ± 25.51 Å²), indicating greater surface burial. In α-glucosidase (Figure 13B), compound 78 showed the lowest SASA (mean = 73.75 ± 31.06 Å²), whereas compound 61 displayed transient expansion before stabilization (mean = 192.59 ± 42.56 Å²); the control remained intermediate (mean = 114.12 ± 12.78 Å²). MolSA further [83]supported enhanced complex stability, as lower values denote tighter structural packing (Additional file 2, Figure SF7). In both enzymes, selected ligands demonstrated markedly lower MolSA than the control (α-amylase (mean): compound 61 = 314.29 ± 1.36 $Å^2$, compound 88 = 277.20 ± 1.36 $Å^2$, and control = 506.38 ± 5.05 $Å^2$; α-glucosidase (mean): compound 61 = 314.57 ± 1.29 $Å^2$, compound 78 = 356.26 ± 3.27 $Å^2$ and control = 515.39 ± 4.88 $Å^2$). PSA analysis (Additional file 2, Figure SF7) revealed consistently lower values for the selected compounds relative to the control, suggesting improved membrane permeability [84, 85] (α-amylase (mean): compound 61 = 105.86 ± 1.98 $Å^2$, compound 88 = 117.44 ± 2.46 $Å^2$, and control = 507.20 ± 12.86 $Å^2$; α-glucosidase (mean): compound 61 = 106.18 ± 2.12 $Å^2$, compound 78 = 237.80 ± 6.90 $Å^2$ and control = 536.11 ± 12.07 $Å^2$).

3.9.9.5 Hydrogen bond analysis

Hydrogen-bond analysis was performed to assess ligand stability at the active site and its impact on intraprotein hydrogen-bond networks, a key determinant of molecular recognition and interaction specificity [80] (Figure 13C, D). In α amylase, compound 61 exhibited minimal deviation from the apo form (apo (mean): 468.60 ± 9.21; compound 61 (mean): 467.62 ± 8.31),

indicating preservation of the native hydrogen-bonding network without substantial polar rearrangement. A similar trend was observed in α-glucosidase (apo (mean): 600.50 ± 11.16; compound 61 (mean): 600.70 ± 12.50). In contrast, compound 88 in α-amylase (mean = 460.25 ± 11.42) and compound 78 in α-glucosidase (mean = 595.51 ± 15.01) reduced the total number of intraprotein hydrogen bonds and increased dynamic variability, suggesting ligand-induced local reorganization. The control slightly reduced hydrogen bonding in α-amylase (mean = 465.46 ± 9.47) but increased it in α-glucosidase (mean = 616.80 ± 9.63) with the lowest variability, indicating differential stabilization effects across targets.

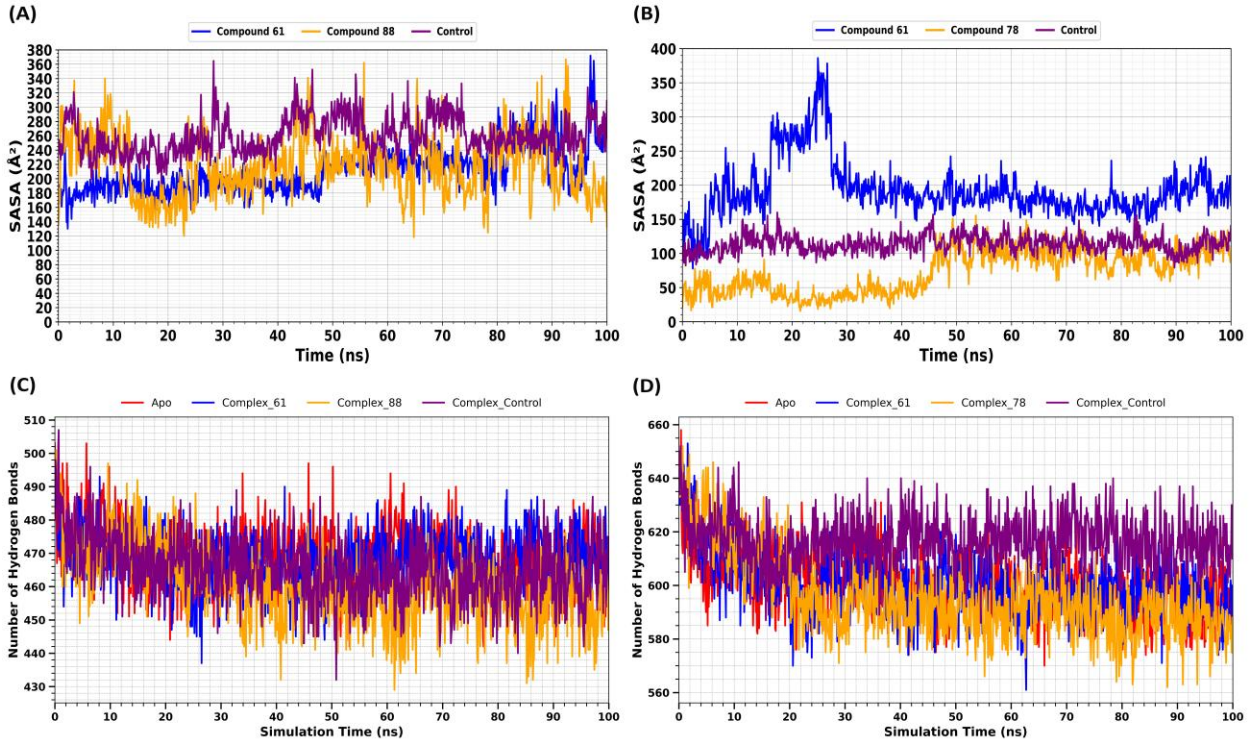


Figure 13: Solvent-accessible surface area (SASA) and hydrogen-bond analyses of selected GC–MS identified compounds from the methanolic extract of *H. fomes* leaves (MEHFL) in α-amylase and α glucosidase. (A, B) SASA profiles; (C, D) hydrogen-bond dynamics for α-amylase and α glucosidase, respectively.

3.9.9.6 Protein-ligand contact analysis

A comprehensive protein–ligand contact analysis was performed over the 100 ns MD trajectories to characterize interaction persistence (Figure 14). In α amylase, compound 61 demonstrated prominent interactions with TRP58, TRP59, GLN63, THR163, and HIS305, reflected by high interaction fractions. GLN63 maintained hydrogen bonding for ~90% of the simulation. In α glucosidase, compound 61 primarily formed ionic interactions, with ASP242, HIS280, and PRO312 showing occupancies >0.7. Compound 88 (α amylase) and compound 78 (α glucosidase) exhibited interaction networks largely dominated by hydrogen bonds. For compound 88, key residues included TRP59, GLN63, and ASP53. For compound 78, TYR158, GLN279, GLU411, and SER311 were predominant, with GLU411 forming hydrogen bonds for ~99% of the trajectory. The control displayed comparatively more extensive and persistent interaction profiles in both enzymes. In α amylase, major contacts involved TYR59, GLN63, ALA106, THR163, ASP197, and ASP300. In α glucosidase, dominant interactions were observed with ASP242, GLU277, ASP307, ASP352, ASN350, and GLU411.

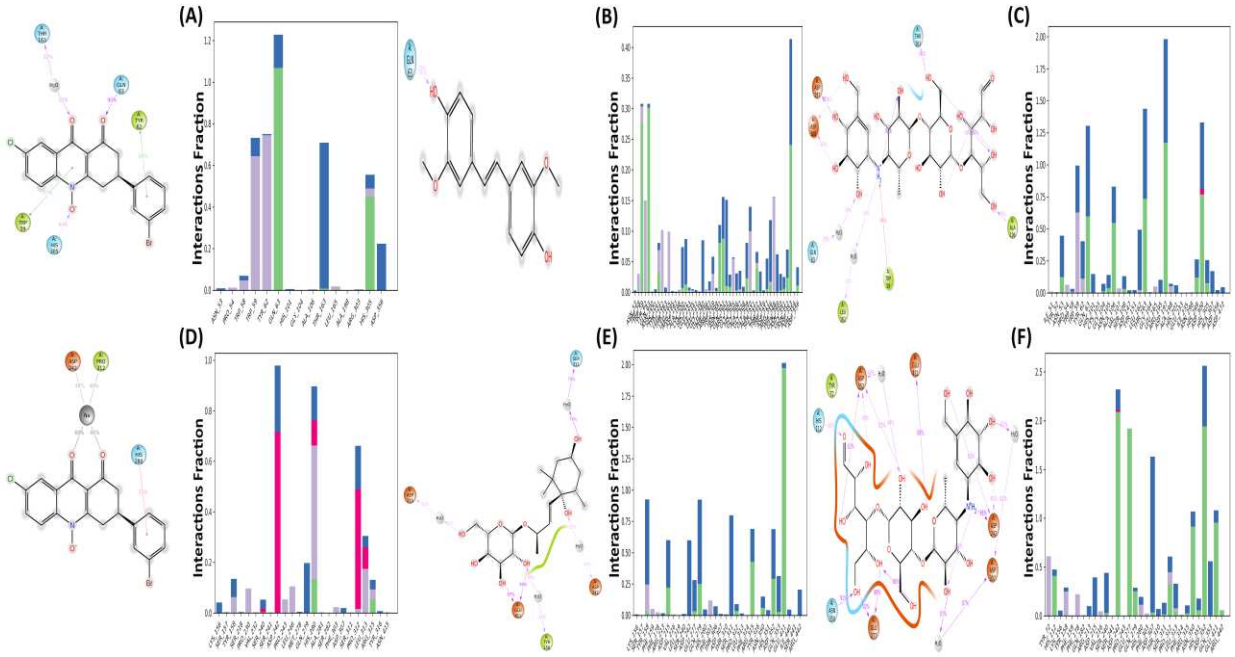


Figure 14: Protein–ligand contact profiling of selected GC–MS identified compounds from the methanolic extract of *H. fomes* leaves (MEHFL) in α-amylase and α glucosidase. The upper panel illustrates interactions of (A) compound 61, (B) compound 88, and (C) the control with α amylase. The lower panel presents interactions of (D) compound 61, (E) compound 78, and (F) the control with α glucosidase. For each representation, two-dimensional interaction maps (left) are accompanied by corresponding interaction fraction plots (right).

3.9.10 Post simulation MM-GBSA analysis

Post-simulation MM-GBSA analysis was performed to elucidate the thermodynamic stability of the protein–ligand complexes (Table 6). In α amylase, compound 61 exhibited its most favorable binding at 50 ns (ΔG_{Bind} = −34.52 kJ/mol), driven by van der Waals (−25.50 kJ/mol) and Coulombic (−6.32 kJ/mol) contributions that offset the polar solvation penalty (+18.15 kJ/mol). At 100 ns, despite improved vdW interactions (−29.68 kJ/mol), increased electrostatic and solvation contributions attenuated overall binding (ΔG_{Bind} = −26.50 kJ/mol), suggesting transient

stabilization. Compound 88 displayed weaker early binding but improved at 100 ns (ΔG_{Bind} = −23.83 kJ/mol), consistent with optimized hydrophobic accommodation. The control showed the least stable profile, with the weakest binding at 100 ns (−15.72 kJ/mol). In α glucosidase, compound 61 demonstrated consistent moderate binding across the trajectory. Compound 78 exhibited the most favorable energetics at 100 ns (ΔG_{Bind} = −36.27 kJ/mol), driven by strong vdW (−29.36 kJ/mol) and Coulombic (−26.12 kJ/mol) interactions despite solvation penalties (+17.26 kJ/mol), indicating robust electrostatic and hydrophobic stabilization upon relaxation. The control displayed variable behavior, with moderate binding at 100 ns (−28.71 kJ/mol) primarily supported by favorable vdW contributions.

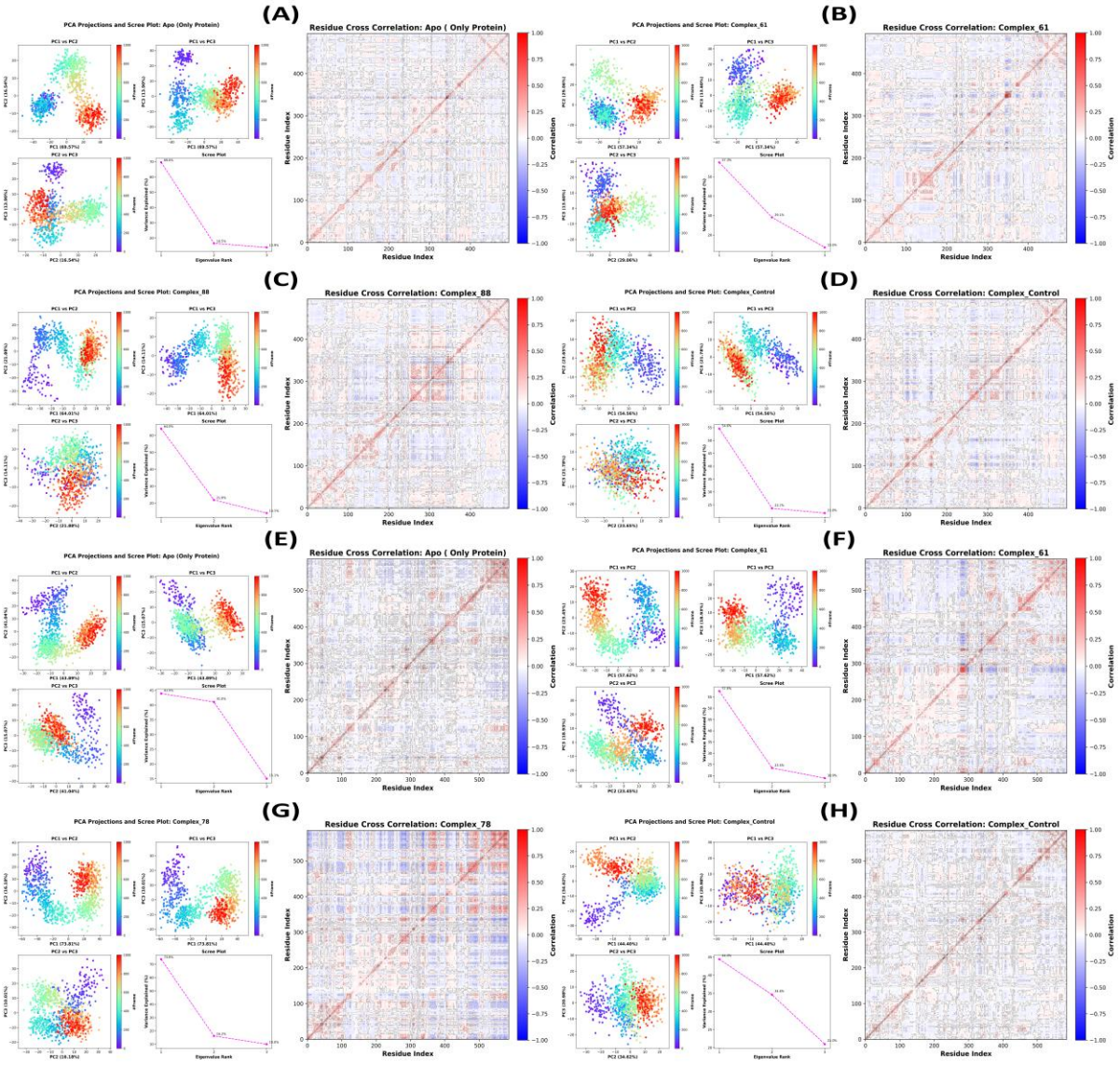
Table 6: Prime MM–GBSA energy components and total binding free energies (kJ/mol) computed from snapshots at 0, 50, and 100 ns for the apo forms of α-amylase and α-glucosidase and their complexes with selected GC–MS-identified compounds from the methanolic extract of *H. fomes* leaves (MEHFL) and the control ligand.

Protein name	Ligand	Simulation time	ΔG_{Bind} (KJ/mol)	$\Delta G_{BindCoulomb}$ (KJ/mol)	$\Delta G_{BindCovalent}$ (KJ/mol)	$\Delta G_{BindHbond}$ (KJ/mol)	$\Delta G_{BindLipo}$ (KJ/mol)	$\Delta G_{BindPacking}$ (KJ/mol)	$\Delta G_{BindSolvGB}$ (KJ/mol)	$\Delta G_{BindvdW}$ (KJ/mol)
α amylase	Apo	0 ns	−19.64	−9.96	3.89	−2.81	−4.52	−2.84	15.9	−33.55
		50 ns	−32.61	−15.06	3.24	−1.32	−4.94	−1.84	16.73	−21.88
		100 ns	−31.83	−2.67	2.22	−2.79	−2.35	−2.75	24.85	−21.71
	Compound 61	0 ns	−29.42	−13.54	2.20	−1.12	−6.67	−1.12	24.75	−26.13
		50 ns	−34.52	−6.32	1.39	−1.80	−2.40	−2.49	18.15	−25.50
		100 ns	−26.50	−23.68	1.77	−0.13	−3.21	−2.19	20.40	−29.68
	Compound 88	0 ns	−14.61	2.51	−2.14	−1.22	−1.02	16.21	−32.17	−14.61
		50 ns	−10.12	1.26	−1.67	−1.75	−0.61	25.12	−27.60	−10.12
		100 ns	−23.83	−4.06	0.77	−5.01	−1.56	19.99	−19.42	−23.83
	Control	0 ns	−26.25	−6.94	2.69	−2.71	−4.56	−1.25	12.72	−23.58
		50 ns	−27.72	−7.70	3.82	−1.88	−5.52	−2.26	17.44	−25.13
		100 ns	−15.72	−14.02	2.03	−1.67	−8.43	−2.75	22.65	−30.91
α glucosidase	Apo	0 ns	−30.30	−19.21	−1.24	−1.07	−7.24	−1.78	19.91	−19.62
		50 ns	−38.12	−30.52	−0.11	−2.59	−5.01	−0.43	25.44	−25.92
		100 ns	−22.46	−26.45	2.68	−2.86	−1.90	−2.14	25.00	−30.49
	Compound 61	0 ns	−30.50	−14.97	3.01	−1.04	−5.24	−1.11	17.63	−27.27
		50 ns	−31.63	−7.66	3.14	−1.21	−5.22	−2.41	23.17	−28.14
		100 ns	−28.98	−9.57	3.89	−1.52	−3.89	−2.33	20.58	−26.19
	Compound 78	0 ns	−24.39	−26.20	1.50	−1.17	−6.84	−1.64	9.55	−21.39
		50 ns	−32.93	1.17	3.74	−3.27	−7.83	−2.37	18.66	−32.23
		100 ns	−36.27	−26.12	−0.53	−2.01	−3.76	−1.56	17.26	−29.36
	Control	0 ns	−31.66	−24.95	2.76	−1.80	−3.24	0.37	9.99	−25.11
		50 ns	−23.77	1.69	1.40	−1.16	−0.43	−1.08	31.07	−24.94
		100 ns	−28.71	−13.54	0.75	−1.55	−9.35	−1.02	18.19	−34.43

3.9.11 PCA and DCCM analysis

Principal component analysis (PCA) delineated the dominant collective motions and major conformational variances across all systems (Figure 15). The first three principal components (PC1–PC3) captured the majority of structural fluctuations. Distinct clustering patterns revealed ligand-specific modulation of conformational landscapes, indicating differential dynamic reprogramming by MEHFL-derived phytochemicals. In α amylase, compound 61 redistributed conformational sampling beyond the apo PC1 space (PC1: compound 61 = −37.90, apo = −52.77), shifting population toward PC2 and suggesting localized induced-fit adaptation rather than rigidification. Compound 88 restricted global conformational space (PC1: −45.47), consistent with partial dynamic confinement. In contrast, the control markedly suppressed intrinsic apo motions (PC1: −21.09), stabilizing a narrow conformational ensemble. In α glucosidase, compound 61 modestly enhanced collective flexibility relative to the apo state (PC1: compound 61 = −32.52, apo = −30.48), whereas compound 78 induced pronounced large-scale rearrangement (PC1: −58.98), indicative of a strong induced-fit mechanism. The control exhibited mild rigidification (PC1: −28.81), limiting conformational diversity compared with phytochemical-bound states. DCCM analysis was performed to elucidate ligand-induced modulation of residue–residue dynamic coupling (Figure 15). In α amylase, compound 61 enhanced localized positive correlations while attenuating extreme anti-correlations observed in the apo state, indicating stabilization of a coordinated residue network and suppression of intrinsic functional transitions which is consistent with a plausible inhibitory mechanism. Compound 88 induced moderate, distributed redistribution of correlations across multiple residue pairs, reflecting global but subtle dynamic rewiring. The control ligand also reshaped correlation patterns; however, it reduced extremes without generating the pronounced correlation hotspots observed with compound 61. In

α glucosidase, compound 61 intensified both correlated and anti-correlated motions, suggesting the emergence of strong localized coupling and opposing residue networks, potentially indicative of newly established allosteric communication pathways. Compound 78 promoted broad, system-wide reorganization of dynamic coupling, consistent with large-scale conformational rearrangement and formation of an inhibited conformational ensemble. In contrast, the control reduced overall coupling while retaining a limited number of dominant correlated residue pairs.



838

839 **Figure 15:** Principal component analysis (PCA) and dynamic cross-correlation matrix (DCCM)
840 analyses of α-amylase and α-glucosidase in their apo forms and in complex with selected GC–MS
841 identified compounds from the methanolic extract of *H. fomes* leaves (MEHFL). (A–D) represent
842 the PCA and DCCM results for the apo protein, compound 61, compound 88, and the control
843 complex with α amylase, respectively. (E–H) illustrate the corresponding PCA and DCCM
844 analyses for the apo protein, compound 61, compound 78, and the control complex with α
845 glucosidase.

3.9.12 Free energy landscape (FEL) analysis

Energy transitions, structural stability, and dynamic behavior of the protein–ligand complexes were evaluated using Rg–RMSD based FEL analysis (Figure 16). Rg reflects global compactness, whereas RMSD represents conformational deviation. The FEL provides a thermodynamic topography in which deep basins correspond to stable conformational states and elevated regions denote energy barriers between transitions. The α-amylase apo form populates a single dominant basin with moderate RMSD dispersion. Compound 61 slightly shifts the basin toward higher RMSD with a narrower distribution, indicating mild backbone mobilization while maintaining ensemble compactness. Compound 88 generates a confined RMSD basin with marginally increased Rg, suggesting a stabilized yet slightly expanded conformational state. The control exhibits the strongest rigidification, characterized by a deep, narrow basin at lower Rg. In α glucosidase, the apo structure occupies a relatively tight basin. Compound 61 broadens the landscape, increasing Rg and RMSD dispersion, indicative of enhanced conformational heterogeneity. Compound 78 further expands sampling, producing a broad, shallow basin consistent with large-scale structural rearrangement. Conversely, the control markedly stabilizes the enzyme, yielding a deep, narrow basin with minimal conformational dispersion.

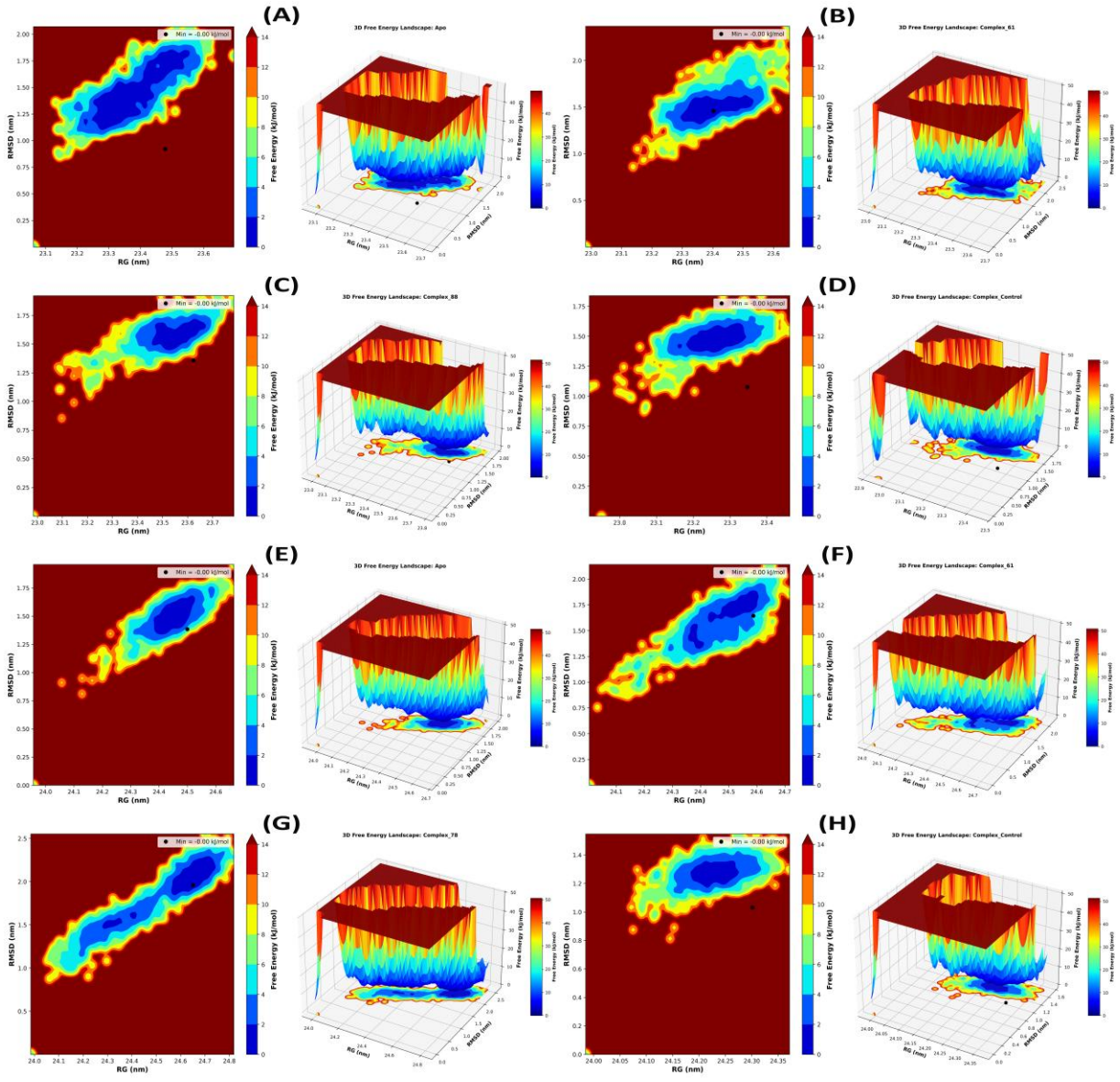
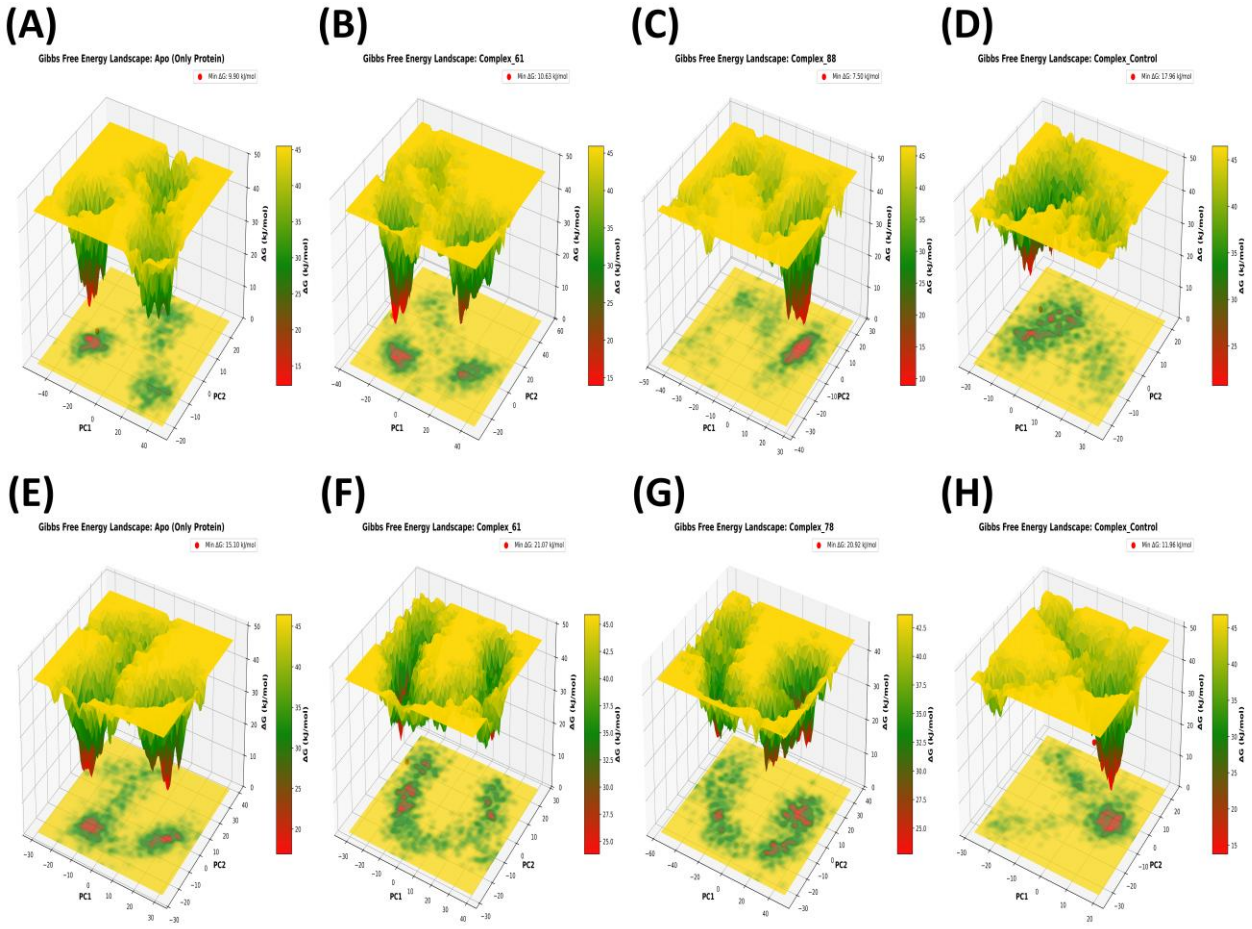


Figure 16: Rg–RMSD based FEL analysis of α-amylase and α-glucosidase in their apo forms and in complex with selected GC–MS identified compounds from the methanolic extract of *H. fomes* leaves (MEHFL). (A–D) depict the FEL profiles of the apo protein, compound 61, compound 88, and the control complex with α amylase, respectively. (E–H) present the corresponding FEL analyses for the apo protein, compound 61, compound 78, and the control complex with α glucosidase. In each case, the left side illustrates the two-dimensional FEL projection, whereas the right side presents the corresponding three-dimensional energy basin representation.

3.9.13 Gibbs free energy landscape analysis

Ligand-induced conformational redistribution was characterized using FELs projected onto the first two principal components (PC1 and PC2) (Figure 17). In α amylase, compound 88 stabilizes a distinct conformational basin spatially separated from the apo minimum, with a deeper free energy well, indicating stabilization of a thermodynamically favorable alternative state. In contrast, compound 61 shifts the conformational ensemble toward a nearby basin that is slightly less favorable than the apo minimum, suggesting modest population redistribution without substantial energetic stabilization. The control exhibits a global minimum ($\Delta G = -17.96$ kJ/mol) that is less favorable than both the apo and ligand-bound states, indicating comparatively weaker thermodynamic stabilization within the PC1–PC2 projection. In α glucosidase, compound 61 displays the least favorable minimum ($\Delta G = -20.92$ kJ/mol), directing the protein toward a remote, high–free energy conformational region, consistent with low-occupancy states. Compound 78 promotes sampling of an alternative PC space; however, this basin remains thermodynamically less favorable than the apo and control minima. Notably, the control exhibits the lowest ΔG (-11.96 kJ/mol), stabilizing a comparatively favorable conformational state primarily along PC2.



886 **Figure 17:** Gibbs free energy landscape (FEL) analysis of α-amylase and α-glucosidase in their
887 apo states and in complex with selected GC–MS–identified compounds from the methanolic
888 extract of *H. fomes* leaves (MEHFL). (A–D) illustrate the FEL profiles of the apo enzyme,
889 compound 61, compound 88, and the control complex with α amylase, respectively. (E–H) show
890 the corresponding FEL profiles for the apo enzyme, compound 61, compound 78, and the control
891 complex with α glucosidase.

892

893

4. Discussion

Type 2 diabetes mellitus (T2DM) is a complex, multifactorial, polygenic disorder and a major global public health challenge, currently ranking ninth among the leading causes of mortality worldwide [2, 5]. This multisystem metabolic disease is characterized by persistent hyperglycemia resulting from insulin resistance and progressive pancreatic β-cell dysfunction. Its pathogenesis involves interconnected mechanisms, including β-cell dedifferentiation, mitochondrial dysfunction, oxidative stress, and chronic low-grade inflammation [86]. Multiple pharmacological agents targeting distinct pathophysiological pathways are available for the management of type 2 diabetes mellitus [6]. Suppression of postprandial hyperglycemia, primarily through inhibition of intestinal α-amylase and α glucosidase, remains a key therapeutic strategy, as chronic hyperglycemia drives diabetic complications [87]. Although currently approved enzyme inhibitors effectively attenuate postprandial glucose excursions, their clinical use is limited by gastrointestinal adverse effects [88, 89]. Plant derived secondary metabolites have historically served as important sources of drug leads [90]. Despite their rich ethnopharmacological relevance and structural diversity, many mangrove species remain insufficiently explored with respect to pharmacological activity and metabolite characterization [18, 19]. Therefore, the present study employed integrated experimental and computational approaches to evaluate the antioxidant, anti-inflammatory, and antidiabetic potential of *H. fomes* leaves, perform comprehensive metabolite profiling, and identify candidate α-amylase and α-glucosidase inhibitory lead compounds.

Preliminary qualitative phytochemical screening provided baseline insight into the composition of MEHFL. The analysis revealed the presence of diverse classes of bioactive constituents associated with a broad spectrum of pharmacological activities [91–96]. Such qualitative approaches are simple, cost effective, and accessible, serving as an initial foundation for subsequent detailed

phytochemical and bioactivity investigations [97]. Quantitative analysis identified phenolics as the predominant constituents, whereas flavonoids were present at lowest levels, likely reflecting solvent selectivity, as absolute methanol preferentially extracts lower molecular weight polyphenols over flavonoids [98–100]. The high phenolic content support the pronounced in vitro antioxidant, anti-inflammatory, and antidiabetic activities observed. [15, 98]. MEHFL demonstrated dose dependent antioxidant activity in both DPPH radical scavenging and ferricyanide reducing power assays, surpassing ascorbic acid, indicating the presence of hydrophobic and hydrophilic antioxidants capable of neutralizing free radicals and enhancing redox balance [101–104]. MEHFL demonstrated dose-dependent inhibition of protein denaturation and superior anti-inflammatory activity relative to the positive controls, suggesting potential efficacy in mitigating persistent subclinical inflammation [105]. Furthermore, MEHFL significantly inhibited α-amylase and α-glucosidase in vitro, exceeding the effect of acarbose. Such dual enzyme inhibition may enhance postprandial glycemic control by simultaneously suppressing starch hydrolysis and glucose release. [106–108]. Given that chronic hyperglycemia, oxidative stress, and inflammation are central to the progression of T2DM and its complications [4], the observed bioactivities of MEHFL support its therapeutic potential in the management of T2DM and related complications.

Preclinical toxicity evaluation of MEHFL was performed using the brine shrimp lethality bioassay and acute oral toxicity testing to ensure safety prior to in vivo experimentation [109, 110]. The brine shrimp assay demonstrated moderate cytotoxic activity, suggesting the presence of biologically active constituents, while the comparatively higher LC_{50} value relative to the control indicated an acceptable safety margin within therapeutic ranges [111, 112]. The detected phenolic constituents may partially account for the observed bioactivity [112]. Acute oral toxicity

assessment, conducted according to OECD guideline 423, classified MEHFL under category 5, indicating low acute toxicity [113]. Transient behavioral alterations observed in the murine model, in the absence of mortality, are consistent with outcomes commonly reported under OECD guideline 423 and suggest reversible functional effects rather than systemic toxicity [114, 115]. Collectively, these findings informed the selection of appropriate dose levels for subsequent in vivo experiments.

In vivo antidiabetic evaluations were conducted to assess the insulin sensitizing and potential β cell restorative effects of MEHFL in established diabetic models. Together, these assays enabled assessment of both acute glucose tolerance and sustained glycemic control [116]. MEHFL produced dose dependent antihyperglycemic effects in both models, with the higher dose demonstrating greater efficacy than metformin. In the OGTT, which reflects glucose utilization and insulin responsiveness [117], MEHFL improved glycemic control, suggesting enhanced peripheral glucose uptake or modulation of insulin sensitivity [43]. In the alloxan induced diabetic model, hyperglycemia results from selective pancreatic β cell destruction mediated by oxidative stress and free radical generation [118]. Alloxan induced β cell damage triggers inflammatory signaling cascades, including NFκB activation and inflammasome mediated responses, thereby perpetuating oxidative inflammatory cycles [119]. The observed in vivo antihyperglycemic activity of MEHFL may be attributed to its α-amylase and α-glucosidase inhibitory properties, along with its antioxidant and anti-inflammatory effects, which may mitigate oxidative and inflammatory damage. These findings are consistent with previous reports [21, 22, 120–122] and support the therapeutic potential of MEHFL in diabetes management.

Comprehensive metabolite profiling of MEHFL was performed using FTIR and GC–MS analyses [123]. FTIR spectroscopy provided functional group fingerprints that corroborated the results of

963 preliminary qualitative and quantitative phytochemical screening, confirming a phenolic rich
964 extract. These observations are consistent with previous reports [124]. GC–MS analysis enabled
965 the identification of individual constituents, with rhodopin detected as the most abundant
966 compound, consistent with its reported occurrence in related mangrove species [125]. Although
967 phytochemical screening and FTIR indicated high phenolic content, the GC–MS chromatogram
968 was dominated by other classes of secondary metabolites. This apparent discrepancy likely reflects
969 methodological constraints, as comprehensive phenolic characterization often requires
970 complementary analytical techniques [126, 127]. Importantly, systematic metabolite profiling of
971 *H. fomes* leaves has been limited, and the present study contributes novel and meaningful insights
972 in this context.

973 Following GC–MS guided identification of 97 secondary metabolites from MEHFL, structure
974 based virtual screening was conducted against α-amylase and α-glucosidase to identify potential
975 antidiabetic leads. Compound 61, 3- [3-bromophenyl]-7-chloro-3,4-dihydro-10-hydroxy-
976 1,9(2H,10H)-acridinedione, emerged as a promising dual inhibitor, exhibiting superior binding
977 affinity to acarbose and comparable interaction profiles. The compound satisfied Lipinski criteria
978 and demonstrated favorable physicochemical, ADME, permeability, and toxicity predictions,
979 although potential cytochrome P450 interactions suggest drug interaction risk [128, 129]. Off
980 target predictions indicated possible modulation of oxidative stress and inflammation related
981 pathways, including matrix metalloproteinases [73, 74]. Molecular dynamics simulations
982 supported stable binding [130], reinforcing its dual inhibitory potential, while indicating the need
983 for further structural refinement. The development of dual α amylase/α-glucosidase inhibitors
984 offers theoretical and therapeutic advantages over single-target agents by enabling coordinated
985 suppression of carbohydrate digestion and postprandial glucose excursions [131, 132]. In this

context, the identification of Compound 61 as a probable dual inhibitory lead underscores the significance of the present study. Additionally, Compound 88 ((3S,5R,6S,7E,9x)-7-megastigmene-3,6,9-triol 9-glucoside) and Compound 78 ((E)-4,4'-(ethene-1,2-diyl) bis(2-methoxyphenol)) were identified as promising candidates for selective inhibition of α-amylase and α-glucosidase, respectively, based on their binding performance and dynamic stability profiles. Beyond glycemic control, in silico target predictions suggest that these compounds may also contribute to the attenuation of oxidative stress and inflammatory pathways associated with T2DM related complications. Collectively, these findings highlight the therapeutic potential of secondary metabolites derived from *H. fomes* leaves as promising scaffolds for future antidiabetic drug development.

5. Conclusion

Type 2 diabetes mellitus remains a major global public health challenge, associated with substantial healthcare expenditures, morbidity, and mortality. Medicinal plants have long served as valuable sources of structurally diverse scaffolds for drug discovery, including antidiabetic agents. The present study investigated *H. fomes* leaves using integrated experimental and computational approaches to evaluate their therapeutic potential and to identify candidate compounds capable of mitigating chronic hyperglycemia, oxidative stress, and inflammation associated with T2DM. The methanolic leaf extract demonstrated significant antioxidant, anti-inflammatory, and antidiabetic activities in vitro, along with pronounced antihyperglycemic effects in vivo. FTIR and GC–MS analyses characterized its metabolite profile, and subsequent in silico investigations identified three promising lead compounds. Collectively, these findings provide the first comprehensive metabolite profiling of *H. fomes* leaves and computational evidence supporting their potential role in T2DM management.

Despite the strengths of this multifaceted approach, several limitations warrant consideration. The in vitro antidiabetic activity was primarily attributed to inhibition of carbohydrate metabolizing enzymes, which does not fully capture the complex pathophysiology of T2DM. Moreover, the alloxan induced diabetic rat model may not adequately replicate human disease heterogeneity, including genetic, environmental, and dietary influences that affect therapeutic response. The tested concentrations may not directly translate to clinically achievable doses, highlighting the need for dose optimization studies. In vivo evaluation was limited to blood glucose measurements, without assessment of additional biochemical markers or histopathological alterations. Furthermore, although computational analyses facilitated rapid lead identification, experimental validation of the predicted targets and activities remains essential. Future investigations should incorporate comprehensive biochemical and histological assessments, advanced omics based mechanistic studies, and well-designed preclinical and clinical trials to enhance translational relevance. Overall, this study provides valuable insight into the therapeutic potential, metabolite profile, and lead identification of *H. fomes* leaves, thereby establishing a foundation for further advanced investigations.

List of abbreviations

DM: Diabetes mellitus

T2DM: Type 2 diabetes mellitus

MEHFL: Methanolic extract of *Heritiera fomes* leaves

TPC: Total phenolic content

TFC: Total flavonoid content

TTC: Total tannin content

DPPH: 2,2-diphenyl-1-picrylhydrazyl

BSA: Bovine serum albumin

DNSA: 3,5-dinitrosalicylic acid

pNPG: 4-Nitrophenyl α-D-glucopyranoside

DMSO: Dimethyl sulfoxide

ppt: Parts per trillion

OECD: Organization for Economic Cooperation and Development guidelines

API: Active pharmaceutical ingredient

OGTT: Oral glucose tolerance test

FBG: Fasting blood glucose

FTIR: Fourier Transform Infrared Spectroscopy

GC–MS: Gas Chromatography-Mass Spectrometry

NIST: National Institute of Standard and Technology

SEM: Standard error of mean

ANOVA: Analysis of Variance

SMILES: Simplified Molecular Input Line Entry System

SDF: Structure data file

PDB: Protein data bank

ADMET: Absorption, distribution, metabolism, excretion and toxicity

DFT: Density functional theory

HOMO: Highest occupied molecular orbital

LUMO: Lower unoccupied molecular orbital

MEP: Molecular electrostatic potential

MD simulation: Molecular dynamics simulation

RMSD: Root Mean Square Deviation

RMSF: Root Mean Square Fluctuation

Rg: Radius of Gyration

MMGBSA: Molecular Mechanics Generalized Born Surface Area

SASA: Solvent accessible surface area

MolSA: Molecular surface area

PSA: Polar surface area

PCA: Principle component analysis

DCCM: Dynamic Cross-Correlation Matrix

FEL: Free energy landscape

Declarations

Ethics approval and consent to participate

All animal experiments were approved by the Animal Welfare and Experimentation Ethics Committee, Faculty of Biological Sciences, Islamic University, Kushtia-7003, Bangladesh (Approval reference: AWEEC/FOB/IU/2025(12)). Consent to participate is not applicable.

Clinical trial number

Not applicable.

Consent for publication

Not applicable.

Availability of Data and Materials

The experimental datasets generated and/or analyzed during the current study are available from the corresponding author upon reasonable request. All data generated or analyzed as part of the in silico component of this study are included in this published article.

Competing Interests

The authors have no competing interests to declare.

Funding

This research did not receive any specific grant from funding agencies in the public, commercial, or not-for-profit sectors.

Author Contribution

A.P.S. served as the supervisor and principal investigator, conceptualized the study, and performed critical review and editing of the manuscript. M.Sha. designed the study and methodology, conducted the in vitro, in vivo, and bioinformatics assays, performed data curation and statistical

analysis, and prepared the original manuscript. L.H.J.B. and S.N.I.A. contributed to the in vitro, in vivo, and bioinformatics assays, data acquisition, data analysis, and manuscript drafting. M.A.A.M. conducted the molecular dynamics simulation and DFT-based bioinformatics assays, provided the requisite software for molecular dynamics simulation and DFT-based bioinformatics analyses, and contributed to manuscript review and editing. P.R., A.S., F.I., M.R.K., M.S., and M.K.K. participated in data acquisition and analysis, and contributed to manuscript drafting. S.K.K. verified all results and performed critical review of the manuscript. All authors have read, reviewed, and approved the final version of the manuscript.

Acknowledgements

The authors gratefully acknowledge the Department of Pharmacy, Islamic University, Kushtia-7003, Bangladesh and Jahangirnagar University, Savar, Dhaka-1342, Bangladesh for providing a supportive academic environment and necessary resources to conduct this research. The authors also acknowledge BEACON Pharmaceuticals PLC for providing the active pharmaceutical ingredient (API) used in this study.

References

1. Powers AC, Niswender KD, Evans-Molina C. Diagnosis, Classification, and Pathophysiology. Diabetes Mellitus.

2. Lu X, Xie Q, Pan X, Zhang R, Zhang X, Peng G, et al. Type 2 diabetes mellitus in adults: pathogenesis, prevention and therapy. Sig Transduct Target Ther. 2024;9:262. https://doi.org/10.1038/s41392-024-01951-9.

1107 3. IDF Diabetes Atlas 2025. Diabetes Atlas. https://diabetesatlas.org/resources/idf-diabetes-atlas-
1108 2025/. Accessed 23 Feb 2026.

1109 4. Weinberg Sibony R, Segev O, Dor S, Raz I. Overview of oxidative stress and inflammation in
1110 diabetes. Journal of Diabetes. 2024;16:e70014. https://doi.org/10.1111/1753-0407.70014.

1111 5. Vassalle C, Gaggini M. Type 2 Diabetes and Oxidative Stress and Inflammation:
1112 Pathophysiological Mechanisms and Possible Therapeutic Options. Antioxidants. 2022;11:953.
1113 https://doi.org/10.3390/antiox11050953.

1114 6. Dahlén AD, Dashi G, Maslov I, Attwood MM, Jonsson J, Trukhan V, et al. Trends in
1115 Antidiabetic Drug Discovery: FDA Approved Drugs, New Drugs in Clinical Trials and Global
1116 Sales. Front Pharmacol. 2022;12:807548. https://doi.org/10.3389/fphar.2021.807548.

1117 7. Chaudhury A, Duvoor C, Reddy Dendi VS, Kraleti S, Chada A, Ravilla R, et al. Clinical Review
1118 of Antidiabetic Drugs: Implications for Type 2 Diabetes Mellitus Management. Front Endocrinol.
1119 2017;8. https://doi.org/10.3389/fendo.2017.00006.

1120 8. Tahrani AA, Barnett AH, Bailey CJ. Pharmacology and therapeutic implications of current
1121 drugs for type 2 diabetes mellitus. Nat Rev Endocrinol. 2016;12:566–92.
1122 https://doi.org/10.1038/nrendo.2016.86.

1123 9. Shahzad A, Liu W, Hussain S, Ni Y, Cui K, Sun Y, et al. Integrated in vitro, in silico, and in
1124 vivo approaches to elucidate the antidiabetic mechanisms of Cicer arietinum and Hordeum vulgare
1125 extract and secondary metabolites. Sci Rep. 2025;15:6620. https://doi.org/10.1038/s41598-025-
1126 89642-5.

10. Tundis R, Loizzo MR, Menichini F. Natural Products as _-Amylase and _-Glucosidase Inhibitors and their Hypoglycaemic Potential in the Treatment of Diabetes: An Update.

11. Gieroba B, Kryska A, Sroka-Bartnicka A. Type 2 diabetes mellitus – conventional therapies and future perspectives in innovative treatment. Biochemistry and Biophysics Reports. 2025;42:102037. https://doi.org/10.1016/j.bbrep.2025.102037.

12. Sukhikh S, Babich O, Prosekov A, Kalashnikova O, Noskova S, Bakhtiyarova A, et al. Antidiabetic Properties of Plant Secondary Metabolites. Metabolites. 2023;13:513. https://doi.org/10.3390/metabo13040513.

13. Situmorang PC, Zuhra CF, Lutfia A, Pasaribu KM, Hardiyanti R, Nugraha AP. Harnessing phytochemicals to combat diabetes: Insights into molecular pathways and therapeutic advances. Journal of Functional Foods. 2025;128:106799. https://doi.org/10.1016/j.jff.2025.106799.

14. Sonkamble VV, Wagh NS, Pai SR. Role of Plant Secondary Metabolites as Antidiabetic Agents. In: Akhtar MS, Swamy MK, Sinniah UR, editors. Natural Bio-active Compounds: Volume 1: Production and Applications. Singapore: Springer; 2019. p. 529–50. https://doi.org/10.1007/978-981-13-7154-7_18.

15. Deka H, Choudhury A, Dey BK. An Overview on Plant Derived Phenolic Compounds and Their Role in Treatment and Management of Diabetes. J Pharmacopuncture. 2022;25:199–208. https://doi.org/10.3831/KPI.2022.25.3.199.

16. Aryal D, Joshi S, Thapa NK, Chaudhary P, Basaula S, Joshi U, et al. Dietary phenolic compounds as promising therapeutic agents for diabetes and its complications: A comprehensive review. Food Science & Nutrition. 2024;12:3025–45. https://doi.org/10.1002/fsn3.3983.

17. Islam ATMR, Hasan MdM, Islam MdT, Tanaka N. Ethnobotanical study of plants used by the Munda ethnic group living around the Sundarbans, the world's largest mangrove forest in southwestern Bangladesh. Journal of Ethnopharmacology. 2022;285:114853. https://doi.org/10.1016/j.jep.2021.114853.

18. Sadeer NB, Zengin G, Mahomoodally MF. Biotechnological applications of mangrove plants and their isolated compounds in medicine-a mechanistic overview. Critical Reviews in Biotechnology. 2023.

19. Mitra S, Naskar N, Chaudhuri P. A review on potential bioactive phytochemicals for novel therapeutic applications with special emphasis on mangrove species. Phytomedicine Plus. 2021;1:100107. https://doi.org/10.1016/j.phyplu.2021.100107.

20. Mahmud I, Islam MK, Saha S, Barman AK, Rahman MM, Anisuzzman M, et al. Pharmacological and Ethnomedicinal Overview of Heritiera fomes: Future Prospects. International Scholarly Research Notices. 2014;2014:938543. https://doi.org/10.1155/2014/938543.

21. Ansari P, Flatt PR, Harriott P, Abdel-Wahab YHA. Insulin secretory and antidiabetic actions of Heritiera fomes bark together with isolation of active phytomolecules. PLoS ONE. 2022;17:e0264632. https://doi.org/10.1371/journal.pone.0264632.

22. Nayan MdIH, Alam MdM, Jamil MdA, Hossain MdI, Haq I, Hannan JMA. Pharmacological effect of Heritiera fomes on Long Evans rats against Postprandial Hyperglycemia and $(CH_2O)_n$ adsorption in vitro. J Diabetes Metab Disord. 2023;22:189–97. https://doi.org/10.1007/s40200-022-01058-4.

1169 23. Krakowska-Sieprawska A, Kiełbasa A, Rafińska K, Ligor M, Buszewski B. Modern Methods
1170 of Pre-Treatment of Plant Material for the Extraction of Bioactive Compounds. Molecules.
1171 2022;27:730. https://doi.org/10.3390/molecules27030730.

1172 24. Baibuch S, Zema P, Bonifazi E, Cabrera G, Mondragón Portocarrero A del C, Campos C, et
1173 al. Effect of the Drying Method and Optimization of Extraction on Antioxidant Activity and
1174 Phenolic of Rose Petals. Antioxidants. 2023;12:681. https://doi.org/10.3390/antiox12030681.

1175 25. Beraich A, El Farissi H, Cacciola F, El-Shazly M, Yahyaoui MI, Yousra B, et al. Exploring
1176 the healing power of Pistacia lentiscus stems: insights into extraction methods, polyphenolic
1177 composition, and health-promoting activities. International Journal of Environmental Health
1178 Research. 2025;35:439–52. https://doi.org/10.1080/09603123.2024.2359070.

1179 26. Analgesic and anti-inflammatory effects of ethyl acetate fraction of Polygonum cuspidatum in
1180 experimental animals: Immunopharmacology and Immunotoxicology: Vol 34 , No 2 - Get Access.
1181 https://www.tandfonline.com/doi/full/10.3109/08923973.2011.590499. Accessed 25 Feb 2026.

1182 27. Shaikh JR, Patil M. Qualitative tests for preliminary phytochemical screening: An overview.
1183 Int J Chem Stud. 2020;8:603–8. https://doi.org/10.22271/chemi.2020.v8.i2i.8834.

1184 28. Evans WC. Trease and Evans pharmacognosy. 16th ed. Edinburgh New York:
1185 Saunders/Elsevier; 2009.

1186 29. Tawaha K, Alali FQ, Gharaibeh M, Mohammad M, El-Elimat T. Antioxidant activity and total
1187 phenolic content of selected Jordanian plant species. Food Chemistry. 2007;104:1372–8.
1188 https://doi.org/10.1016/j.foodchem.2007.01.064.

30. Phytochemical Characterization and Evaluation of Pharmacological Activities of Leaves of a Mangrove Plant Species - Aegiceras corniculatum (L.) | Semantic Scholar. https://www.semanticscholar.org/paper/Phytochemical-Characterization-and-Evaluation-of-of/88265005b4ffff3d813a2c7ca229b37a11129cf4. Accessed 21 Jan 2026.

31. Hussen EM, Endalew SA. In vitro antioxidant and free-radical scavenging activities of polar leaf extracts of Vernonia amygdalina. BMC Complement Med Ther. 2023;23:146. https://doi.org/10.1186/s12906-023-03923-y.

32. Kumar RS, Rajkapoor B, Perumal P. Antioxidant activities of Indigofera cassioides Rottl. Ex. DC. using various in vitro assay models. Asian Pacific Journal of Tropical Biomedicine. 2012;2:256–61. https://doi.org/10.1016/S2221-1691(12)60019-7.

33. Guleria I, Kumari A, Lacaille-Dubois M-A, Saini AK, Kumar V, Saini RV, et al. In-vitro antimicrobial, antioxidant, anti-inflammatory, and cytotoxic activities of Populus ciliata bark and leaves: A comparative study. South African Journal of Botany. 2022;148:238–50. https://doi.org/10.1016/j.sajb.2022.04.040.

34. Alhakmani F, Kumar S, Khan SA. Estimation of total phenolic content, *in–vitro* antioxidant and anti–inflammatory activity of flowers of *Moringa oleifera*. Asian Pacific Journal of Tropical Biomedicine. 2013;3:623–7. https://doi.org/10.1016/S2221-1691(13)60126-4.

35. Kazeem MI, Adamson JO, Ogunwande IA. Modes of Inhibition of α-Amylase and α-Glucosidase by Aqueous Extract of Morinda lucida Benth Leaf. BioMed Research International. 2013;2013:527570. https://doi.org/10.1155/2013/527570.

36. Bhatia A, Singh B, Arora R, Arora S. In vitro evaluation of the α-glucosidase inhibitory potential of methanolic extracts of traditionally used antidiabetic plants. BMC Complement Altern Med. 2019;19:74. https://doi.org/10.1186/s12906-019-2482-z.

37. Ullah MO, Haque M, Urmi KF, Md. Zulfiker AH, Anita ES, Begum M, et al. Anti–bacterial activity and brine shrimp lethality bioassay of methanolic extracts of fourteen different edible vegetables from Bangladesh. Asian Pacific Journal of Tropical Biomedicine. 2013;3:1–7. https://doi.org/10.1016/S2221-1691(13)60015-5.

38. Sasidharan S, Mordi MohdN, Ismail S, Mansor S, Sahgal G, Ramanathan S. Brine shrimp lethality and acute oral toxicity studies on Swietenia mahagoni (Linn.) Jacq. seed methanolic extract. Phcog Res. 2010;2:215. https://doi.org/10.4103/0974-8490.69107.

39. Jothy SL, Zakaria Z, Chen Y, Lau YL, Latha LY, Sasidharan S. Acute oral toxicity of methanolic seed extract of Cassia fistula in mice. Molecules. 2011;16:5268–82. https://doi.org/10.3390/molecules16065268.

40. Meddah B, Ducroc R, El Abbes Faouzi M, Eto B, Mahraoui L, Benhaddou-Andaloussi A, et al. Nigella sativa inhibits intestinal glucose absorption and improves glucose tolerance in rats. Journal of Ethnopharmacology. 2009;121:419–24. https://doi.org/10.1016/j.jep.2008.10.040.

41. Ahmed MF, Kazim SM, Ghori SS, Mehjabeen SS, Ahmed SR, Ali SM, et al. Antidiabetic Activity of Vinca rosea Extracts in Alloxan-Induced Diabetic Rats. International Journal of Endocrinology. 2010;2010:841090. https://doi.org/10.1155/2010/841090.

42. Aljazzaf B, Regeai S, Elghmasi S, Alghazir N, Balgasim A, Hdud Ismail IM, et al. Evaluation of Antidiabetic Effect of Combined Leaf and Seed Extracts of Moringa oleifera (Moringaceae) on

1230 Alloxan-Induced Diabetes in Mice: A Biochemical and Histological Study. Oxidative Medicine
1231 and Cellular Longevity. 2023;2023:9136217. https://doi.org/10.1155/2023/9136217.

1232 43. Alake J, Ahlidja W, Henneh IT, Kwabil A, Adu KD, Asiamah SA, et al. Bioprospecting the
1233 antidiabetic potential of aqueous seed extract of Allanblackia floribunda Oliv. (Clusiaceae). Food
1234 Chemistry Advances. 2025;8:101071. https://doi.org/10.1016/j.focha.2025.101071.

1235 44. Murali VS, Meena Devi VN, Parvathy P, Murugan M. Phytochemical screening, FTIR spectral
1236 analysis, antioxidant and antibacterial activity of leaf extract of *Pimenta dioica* Linn. Materials
1237 Today: Proceedings. 2021;45:2166–70. https://doi.org/10.1016/j.matpr.2020.10.038.

1238 45. Aguree S, Abagale SA, Sackey I. GC–MS and FTIR Characterization of Bioactive Compounds
1239 in Aqueous Extracts of Terminalia laxiflora Root and Mitragyna inermis Stem Bark. Journal of
1240 Chemistry. 2025;2025:7537345. https://doi.org/10.1155/joch/7537345.

1241 46. Vyas A, Patel PK, Patel S, Dixit N, Sagar S. Unlocking potential topoisomerase-II inhibitors:
1242 ligand-based drug design pipeline integrating pharmacophore mapping, virtual screening,
1243 molecular docking, and ADMET profiling. Chem Pap. 2025;79:5023–38.
1244 https://doi.org/10.1007/s11696-025-04103-7.

1245 47. Branches ADS, da Silva JN, de Oliveira MDL, Bezerra DP, Soares MBP, Costa EV, et al. DFT
1246 calculations, molecular docking, binding free energy analysis and cytotoxicity assay of 7,7-
1247 dimethylaporphine alkaloids with methylenedioxy ring in positions 1 and 2. Computational and
1248 Theoretical Chemistry. 2024;1233:114483. https://doi.org/10.1016/j.comptc.2024.114483.

1249 48. Alhawday F, Alminderej F, Ghannay S, Hammami B, Albadri AEAE, Kadri A, et al. In Silico
1250 Design, Synthesis, and Evaluation of Novel Enantiopure Isoxazolidines as Promising Dual

1251 Inhibitors of α-Amylase and α-Glucosidase. Molecules. 2024;29:305.
1252 https://doi.org/10.3390/molecules29020305.

1253 49. Dej-adisai S, Rais IR, Wattanapiromsakul C, Pitakbut T. Alpha-Glucosidase Inhibitory Assay-
1254 Screened Isolation and Molecular Docking Model from Bauhinia pulla Active Compounds.
1255 Molecules. 2021;26:5970. https://doi.org/10.3390/molecules26195970.

1256 50. Kaur N, Kumar V, Nayak SK, Wadhwa P, Kaur P, Sahu SK. Alpha-amylase as molecular
1257 target for treatment of diabetes mellitus: A comprehensive review. Chemical Biology & Drug
1258 Design. 2021;98:539–60. https://doi.org/10.1111/cbdd.13909.

1259 51. Dirir AM, Daou M, Yousef AF, Yousef LF. A review of alpha-glucosidase inhibitors from
1260 plants as potential candidates for the treatment of type-2 diabetes. Phytochem Rev. 2022;21:1049–
1261 79. https://doi.org/10.1007/s11101-021-09773-1.

1262 52. RCSB PDB: Homepage. https://www.rcsb.org/. Accessed 25 Jan 2026.

1263 53. Guex N, Peitsch MC, Schwede T. Automated comparative protein structure modeling with
1264 SWISS-MODEL and Swiss-PdbViewer: A historical perspective. Electrophoresis. 2009;30
1265 SUPPL. 1:162–73. https://doi.org/10.1002/elps.200900140.

1266 54. Farooq A, Mateen RM, Ali M, Javed M, Dera AA, Asimov A, et al. Detection of probable
1267 phytochemical inhibitors targeting kallikrein related peptidase 7 (KLK7) in ovarian cancer through
1268 molecular dynamics and virtual screening approaches. Sci Rep. 2025;15:34749.
1269 https://doi.org/10.1038/s41598-025-18364-5.

55. Wiederstein M, Sippl MJ. ProSA-web: interactive web service for the recognition of errors in three-dimensional structures of proteins. Nucleic Acids Research. 2007;35 Web Server:W407–10. https://doi.org/10.1093/nar/gkm290.

56. Polák L, Škoda P, Riedlová K, Krivák R, Novotný M, Hoksza D. PrankWeb 4: a modular web server for protein–ligand binding site prediction and downstream analysis. Nucleic Acids Research. 2025;53:W466–71. https://doi.org/10.1093/nar/gkaf421.

57. Dallakyan S, Olson AJ. Small-Molecule Library Screening by Docking with PyRx. In: Hempel JE, Williams CH, Hong CC, editors. Chemical Biology: Methods and Protocols. New York, NY: Springer; 2015. p. 243–50. https://doi.org/10.1007/978-1-4939-2269-7_19.

58. Shahroz MM, Sharma HK, Altamimi ASA, Alamri MA, Ali A, Ali A, et al. Novel and Potential Small Molecule Scaffolds as DYRK1A Inhibitors by Integrated Molecular Docking-Based Virtual Screening and Dynamics Simulation Study. Molecules. 2022;27:1159. https://doi.org/10.3390/molecules27041159.

59. Sharma G, Kumar N, Sharma CS, Alqahtani T, Tiruneh YK, Sultana S, et al. Identification of promising SARS-CoV-2 main protease inhibitor through molecular docking, dynamics simulation, and ADMET analysis. Sci Rep. 2025;15:2830. https://doi.org/10.1038/s41598-025-86016-9.

60. Lomize AL, Pogozheva ID. Physics-Based Method for Modeling Passive Membrane Permeability and Translocation Pathways of Bioactive Molecules. J Chem Inf Model. 2019;59:3198–213. https://doi.org/10.1021/acs.jcim.9b00224.

61. Lomize AL, Hage JM, Schnitzer K, Golobokov K, LaFaive MB, Forsyth AC, et al. PerMM: A Web Tool and Database for Analysis of Passive Membrane Permeability and Translocation

1291 Pathways of Bioactive Molecules. J Chem Inf Model. 2019;59:3094–9.
1292 https://doi.org/10.1021/acs.jcim.9b00225.

1293 62. Shabbir F, Mishra VK, Noor S, Nath S, Khan MU, Fawy KF, et al. Computer-aided screening
1294 of marine fungal metabolites as potential inhibitors of new Delhi metallo-beta-lactamase-1. Sci
1295 Rep. 2025;15:33997. https://doi.org/10.1038/s41598-025-12523-4.

1296 63. Fahim AM, Dacrory S, Elsayed GH. Anti-proliferative activity, molecular genetics, docking
1297 analysis, and computational calculations of uracil cellulosic aldehyde derivatives. Sci Rep.
1298 2023;13:14563. https://doi.org/10.1038/s41598-023-41528-0.

1299 64. Kong X, Xiao Z, Chen Y, Du M, Zhang Z, Wang Z, et al. Calcium-binding properties, stability,
1300 and osteogenic ability of phosphorylated soy peptide-calcium chelate. Front Nutr. 2023;10.
1301 https://doi.org/10.3389/fnut.2023.1129548.

1302 65. Genheden S, Ryde U. The MM/PBSA and MM/GBSA methods to estimate ligand-binding
1303 affinities. Expert Opinion on Drug Discovery. 2015;10:449–61.
1304 https://doi.org/10.1517/17460441.2015.1032936.

1305 66. El-Daly MM, Bajrai LH, Alandijany TA, Alsaady IM, Gattan HS, Alhamdan MM, et al.
1306 Exploring Echinacea angustifolia for anti-viral compounds against Zika virus RNA-dependent
1307 RNA polymerase: a computational study. Sci Rep. 2025;15:4060. https://doi.org/10.1038/s41598-
1308 025-88481-8.

1309 67. Abouzied AS, Alqarni S, Younes KM, Alanazi SM, Alrsheed DM, Alhathal RK, et al.
1310 Structural and free energy landscape analysis for the discovery of antiviral compounds targeting

the cap-binding domain of influenza polymerase PB2. Sci Rep. 2024;14:25441. https://doi.org/10.1038/s41598-024-69816-3.

68. Ahmed SS, Rahman MO. From Flora to Pharmaceuticals: 100 new additions to angiosperms of Gafargaon subdistrict in Bangladesh and unraveling antidiabetic drug candidates targeting DPP4 through in silico approach. PLoS ONE. 2024;19:e0301348. https://doi.org/10.1371/journal.pone.0301348.

69. Zhang X, Grabowski B, Körmann F, Ruban AV, Gong Y, Reed RC, et al. Temperature dependence of the stacking-fault Gibbs energy for Al, Cu, and Ni. Phys Rev B. 2018;98:224106. https://doi.org/10.1103/PhysRevB.98.224106.

70. Meyer B, Ferrigni N, Putnam J, Jacobsen L, Nichols D, McLaughlin J. Brine Shrimp: A Convenient General Bioassay for Active Plant Constituents. Planta Med. 1982;45:31–4. https://doi.org/10.1055/s-2007-971236.

71. Tamargo J, Le Heuzey J-Y, Mabo P. Narrow therapeutic index drugs: a clinical pharmacological consideration to flecainide. Eur J Clin Pharmacol. 2015;71:549–67. https://doi.org/10.1007/s00228-015-1832-0.

72. Narrow Therapeutic Index Drugs | DrugBank. https://go.drugbank.com/categories/DBCAT003972. Accessed 25 Feb 2026.

73. Youssef ME, Yahya G, Popoviciu MS, Cavalu S, Abd-Eldayem MA, Saber S. Unlocking the Full Potential of SGLT2 Inhibitors: Expanding Applications beyond Glycemic Control. International Journal of Molecular Sciences. 2023;24:6039. https://doi.org/10.3390/ijms24076039.

74. Winiarska A, Knysak M, Nabrdalik K, Gumprecht J, Stompór T. Inflammation and Oxidative Stress in Diabetic Kidney Disease: The Targets for SGLT2 Inhibitors and GLP-1 Receptor Agonists. International Journal of Molecular Sciences. 2021;22:10822. https://doi.org/10.3390/ijms221910822.

75. Zamanian MY, Alsaab HO, Golmohammadi M, Yumashev A, Jabba AM, Abid MK, et al. NF-κB pathway as a molecular target for curcumin in diabetes mellitus treatment: Focusing on oxidative stress and inflammation. Cell Biochemistry and Function. 2024;42:e4030. https://doi.org/10.1002/cbf.4030.

76. Bonnet F, Scheen AJ. Effects of SGLT2 inhibitors on systemic and tissue low-grade inflammation: The potential contribution to diabetes complications and cardiovascular disease. Diabetes & Metabolism. 2018;44:457–64. https://doi.org/10.1016/j.diabet.2018.09.005.

77. Arabshomali A, Bazzazzadehgan S, Mahdi F, Shariat-Madar Z. Potential Benefits of Antioxidant Phytochemicals in Type 2 Diabetes. Molecules. 2023;28:7209. https://doi.org/10.3390/molecules28207209.

78. Shafiq I, Raza N, Dildar S, Bullo S. Unraveling the NLO potential of isoquinoline functionalized chromophores via molecular modeling using DFT/TD-DFT approaches. Sci Rep. 2025;15:23236. https://doi.org/10.1038/s41598-025-04911-7.

79. Singh JS, Khan MohdS, Uddin S. A DFT study of vibrational spectra of 5-chlorouracil with molecular structure, HOMO–LUMO, MEPs/ESPs and thermodynamic properties. Polym Bull. 2023;80:3055–83. https://doi.org/10.1007/s00289-022-04181-7.

80. Zhang X, Zhang L, Li D, Wang Q, Wang L, Zheng Z, et al. Computational exploration of Eucommia ulmoides flavonoids as potential RANKL inhibitors via molecular docking and dynamics simulations. Sci Rep. 2025;15:17175. https://doi.org/10.1038/s41598-025-01913-3.

81. Sanju SM, Kabir MM, Hossain MI, Rizbi AA, Nadia MN, Ferdous J, et al. Structural and energetic basis of marine phytochemicals as dengue NS1 protein inhibitors. Sci Rep. 2025;15:34162. https://doi.org/10.1038/s41598-025-15030-8.

82. Samad A, Ajmal A, Mahmood A, Khurshid B, Li P, Jan SM, et al. Identification of novel inhibitors for SARS-CoV-2 as therapeutic options using machine learning-based virtual screening, molecular docking and MD simulation. Front Mol Biosci. 2023;10. https://doi.org/10.3389/fmolb.2023.1060076.

83. Ferdausi N, Islam S, Rimti F, Quayum S, Arshad E, Ibnat A, et al. Point-specific interactions of isovitexin with the neighboring amino acid residues of the hACE2 receptor as a targeted therapeutic agent in suppressing the SARS-CoV-2 influx mechanism. J Adv Vet Anim Res. 2022;9:230. https://doi.org/10.5455/javar.2022.i588.

84. Krarup LH, Christensen IT, Hovgaard L, Frokjaer S. Predicting Drug Absorption from Molecular Surface Properties Based on Molecular Dynamics Simulations. Pharm Res. 1998;15:972–8. https://doi.org/10.1023/A:1011905522110.

85. Jia S, Lai H, Chen X, Lu J, Ding W, Cui D, et al. In Silico Identification of the NLRP3 Inhibitors from Traditional Chinese Medicine. International Journal of Molecular Sciences. 2025;26:10569. https://doi.org/10.3390/ijms262110569.

86. Młynarska E, Czarnik W, Dzieża N, Jędraszak W, Majchrowicz G, Prusinowski F, et al. Type 2 Diabetes Mellitus: New Pathogenetic Mechanisms, Treatment and the Most Important Complications. IJMS. 2025;26:1094. https://doi.org/10.3390/ijms26031094.

87. Kashtoh H, Baek K-H. Recent Updates on Phytoconstituent Alpha-Glucosidase Inhibitors: An Approach towards the Treatment of Type Two Diabetes. Plants. 2022;11:2722. https://doi.org/10.3390/plants11202722.

88. Akmal M, Patel P, Wadhwa R. Alpha Glucosidase Inhibitors. In: StatPearls. Treasure Island (FL): StatPearls Publishing; 2025.

89. Marzouk MA, Mahmoud EM, Shehab WS, Fawzy SM, Mohammed SM, Abdel-Razek MA, et al. Dual α-amylase and α-glucosidase inhibition by 1,2,4-triazole derivatives for diabetes treatment. Sci Rep. 2025;15:27172. https://doi.org/10.1038/s41598-025-11214-4.

90. Bhatti MZ, Ismail H, Kayani WK, Bhatti MZ, Ismail H, Kayani WK. Plant Secondary Metabolites: Therapeutic Potential and Pharmacological Properties. In: Secondary Metabolites - Trends and Reviews. IntechOpen; 2022. https://doi.org/10.5772/intechopen.103698.

91. Chintada V, Golla N. Exploring the Therapeutic Potential of Bioactive Compounds from Plant Sources. In: Devi J, editor. Biotechnological Intervention in Production of Bioactive Compounds: Biosynthesis, Characterization and Applications. Cham: Springer Nature Switzerland; 2025. p. 229–47. https://doi.org/10.1007/978-3-031-76859-0_15.

92. Melo LFM de, Aquino-Martins VG de Q, Silva AP da, Oliveira Rocha HA, Scortecci KC. Biological and pharmacological aspects of tannins and potential biotechnological applications. Food Chemistry. 2023;414:135645. https://doi.org/10.1016/j.foodchem.2023.135645.

93. Zhao L, Zheng L. A Review on Bioactive Anthraquinone and Derivatives as the Regulators for ROS. Molecules. 2023;28:8139. https://doi.org/10.3390/molecules28248139.

94. Spriha SE, Rahman SA. A Review on Biological Activities of Sugars and Sugar Derivatives. Dhaka Univ J Pharm Sci. 2022;:381–94. https://doi.org/10.3329/dujps.v20i3.59803.

95. Desai SD, Desai DG, Kaur H. Saponins and their Biological Activities. 2009;41.

96. Dembitsky VM. Biological Activity and Structural Diversity of Steroids Containing Aromatic Rings, Phosphate Groups, or Halogen Atoms. Molecules. 2023;28:5549. https://doi.org/10.3390/molecules28145549.

97. Maheshwaran L, Nadarajah L, Senadeera SPNN, Ranaweera CB, Chandana AK, Pathirana RN. Phytochemical Testing Methodologies and Principles for Preliminary Screening/ Qualitative Testing. Asian Plant Research Journal. 2024;12:11–38. https://doi.org/10.9734/aprj/2024/v12i5267.

98. Rawal P, Pandey B, Yadav RK, Panta S. Antioxidant, Alpha-Amylase Inhibitory and Hypoglycemic Activity of Smallanthus sonchifolius Leaves from Nepal: An Integrated In Vitro, In Vivo, and In Silico Approach. Food Science & Nutrition. 2025;13:e4672. https://doi.org/10.1002/fsn3.4672.

99. Dai J, Mumper RJ. Plant Phenolics: Extraction, Analysis and Their Antioxidant and Anticancer Properties. Molecules. 2010;15:7313–52. https://doi.org/10.3390/molecules15107313.

100. Xiang Z, Liu L, Xu Z, Kong Q, Feng S, Chen T, et al. Solvent Effects on the Phenolic Compounds and Antioxidant Activity Associated with Camellia polyodonta Flower Extracts. ACS Omega. 2024;9:27192–203. https://doi.org/10.1021/acsomega.4c01321.

101. Syed Mohamad SNA, Khatib A, So'ad SZM, Ahmed QU, Ibrahim Z, Nipun TS, et al. In Vitro Anti-Diabetic, Anti-Inflammatory, Antioxidant Activities and Toxicological Study of Optimized Psychotria malayana Jack Leaves Extract. Pharmaceuticals. 2023;16:1692. https://doi.org/10.3390/ph16121692.

102. Dose J, Matsugo S, Yokokawa H, Koshida Y, Okazaki S, Seidel U, et al. Free Radical Scavenging and Cellular Antioxidant Properties of Astaxanthin. Int J Mol Sci. 2016;17:103. https://doi.org/10.3390/ijms17010103.

103. Poljsak B. Strategies for Reducing or Preventing the Generation of Oxidative Stress. Oxid Med Cell Longev. 2011;2011:194586. https://doi.org/10.1155/2011/194586.

104. Zhao J, Xu N, Liu H. Quantitative Assessment of the Effects of Reducing Agents on Biological Macromolecules and on the Possible Repair of Oxidative Damage. Biomed Res Int. 2018;2018:5704016. https://doi.org/10.1155/2018/5704016.

105. Cherbal A, Bouabdallah M, Benhalla M, Hireche S, Desdous R. Phytochemical Screening, Phenolic Content, and Anti-Inflammatory Effect of Foeniculum vulgare Seed Extract. Prev Nutr Food Sci. 2023;28:141–8. https://doi.org/10.3746/pnf.2023.28.2.141.

106. Nguyen C-Q, Phien HH, Son NH, Le Dang Q, Phuong LV, Thi N-YN, et al. Pharmacoinformatics model based on the *para*-aminochalcone core to screening dual alpha-amylase/alpha-glucosidase and β-TC-6 inhibitors: Combining experimental and machine learning

for diabetes drug discovery. Journal of Molecular Structure. 2025;1346:143193. https://doi.org/10.1016/j.molstruc.2025.143193.

107. Chaithanya TS, Sabareesh V. Natural Proteolytic Peptide Inhibitors of Alpha-Glucosidase and Alpha-Amylase as a Strategy to Manage Type 2 Diabetes—A Review. Peptide Science. 2026;118:e70017. https://doi.org/10.1002/pep2.70017.

108. Khan F, Khan MV, Kumar A, Akhtar S. Recent Advances in the Development of Alpha-Glucosidase and Alpha-Amylase Inhibitors in Type 2 Diabetes Management: Insights from In silico to In vitro Studies. http://www.eurekaselect.com.

109. Budha Magar A, Shrestha D, Pakka S, Sharma KR. Phytochemistry, Biological, and Toxicity Study on Aqueous and Methanol Extracts of Chromolaena odorata. ScientificWorldJournal. 2023;2023:6689271. https://doi.org/10.1155/2023/6689271.

110. Sangermano F, Masi M, Kumar A, Peravali R, Tuzi A, Cimmino A, et al. In Vitro and In Vivo Toxicity Evaluation of Natural Products with Potential Applications as Biopesticides. Toxins (Basel). 2021;13:805. https://doi.org/10.3390/toxins13110805.

111. Haque MS, Ahmad R, Sarkar BC, Sana M, Saha HR, Sana NK. Integrating bioactivity and molecular simulations to explore the pharmacological landscape of Lagerstroemia speciosa leaf extract. PLOS ONE. 2025;20:e0339566. https://doi.org/10.1371/journal.pone.0339566.

112. Payel IN, Chowdhury MdT, Momen MdSH, Sadia QA, Eshaque NH, Mamun MdJI, et al. Discovery of Bioactive Properties in the Seagrass Ruppia maritima Extract: A Triplatform Assessment of Antioxidant, Antidiabetic, Antibacterial, Cytotoxic, and Analgesic Activities. The Scientific World Journal. 2025;2025:5452807. https://doi.org/10.1155/tswj/5452807.

113. Ramírez-Santos J, Calzada F, Martínez-Rodríguez J, Valdes M, Barbosa E, Velázquez C. Aqueous Extracts and Flavonoids Obtained from Annona cherimola Miller as Antidiabetic Treatments Alone and in Combination with Antidiabetic Drugs: In Vivo and In Silico Studies. Pharmaceuticals. 2025;18:1754. https://doi.org/10.3390/ph18111754.

114. Barbosa M de M, Lima LMA de, Alves WA da S, Lima EKB de, Silva LA da, Silva TD da, et al. In Vitro, Oral Acute, and Repeated 28-Day Oral Dose Toxicity of a Mixed-Valence Polyoxovanadate Cluster. Pharmaceuticals. 2023;16:1232. https://doi.org/10.3390/ph16091232.

115. Kharchoufa L, Bouhrim M, Bencheikh N, El Assri S, Amirou A, Yamani A, et al. Acute and Subacute Toxicity Studies of the Aqueous Extract from Haloxylon scoparium Pomel (Hammada scoparia (Pomel)) by Oral Administration in Rodents. BioMed Research International. 2020;2020:4020647. https://doi.org/10.1155/2020/4020647.

116. Birru EM, Abdelwuhab M, Shewamene Z. Effect of hydroalcoholic leaves extract of Indigofera spicata Forssk. on blood glucose level of normal, glucose loaded and diabetic rodents. BMC Complement Altern Med. 2015;15:321. https://doi.org/10.1186/s12906-015-0852-8.

117. Kuo FY, Cheng K-C, Li Y, Cheng J-T. Oral glucose tolerance test in diabetes, the old method revisited. World J Diabetes. 2021;12:786–93. https://doi.org/10.4239/wjd.v12.i6.786.

118. Melesie Taye G, Bule M, Alemayehu Gadisa D, Teka F, Abula T. In vivo Antidiabetic Activity Evaluation of Aqueous and 80% Methanolic Extracts of Leaves of Thymus schimperi (Lamiaceae) in Alloxan-induced Diabetic Mice. DMSO. 2020;Volume 13:3205–12. https://doi.org/10.2147/DMSO.S268689.

119. Bukhari HA, Afzal M, Al-Abbasi FA, Sheikh RA, Alqurashi MM, Bawadood AS, et al. In vivo and computational investigation of butin against alloxan-induced diabetes via biochemical, histopathological, and molecular interactions. Sci Rep. 2024;14:20633. https://doi.org/10.1038/s41598-024-71577-y.

120. Sarkar BK, Barman SK, Akhter S, Akter R, Das J, Sarkar AP, et al. Evaluation of in vitro anti diabetic activity of two mangrove plant extracts: Heritiera fomes and Sonneratia apetala.

121. Feda FB. Phytochemical and hypoglycemic screening of Heritiera fomes. Thesis. Brac University; 2022.

122. Sultana MS, Golder M, Biswas B, Karmakar UK, Bokshi B, Alam MJ, et al. Antioxidative and Antidiabetic Potentials of the Pneumatophores of Heritiera fomes Buch. Ham. Dhaka University Journal of Pharmaceutical Sciences. 2022;:283–91. https://doi.org/10.3329/dujps.v20i3.59794.

123. Ella Nkogo L-F, Mikala Mouendou MS, Dumarçay S, Edou Engonga P, Gérardin P. Phytochemical Study, FTIR and GC-MS Characterization and Evaluation of the Antioxidant Activity of Letestua durissima Extracts. Forests. 2024;15:429. https://doi.org/10.3390/f15030429.

124. Patra JK, Thatoi H. Anticancer activity and chromatography characterization of methanol extract of Heritiera fomes Buch. Ham., a mangrove plant from Bhitarkanika, India. Orient Pharm Exp Med. 2013;13:133–42. https://doi.org/10.1007/s13596-013-0113-7.

125. Bidve SC. Metabolite Profiling and Principle Component Analysis of a Mangrove Plant Aegiceras Corniculatum L (Blanco). Int J Pharm Pharmacol. 2018;2:1–9. https://doi.org/10.31531/2581-3080.1000125.

126. Saleem A, Afzal M, Naveed M, Makhdoom SI, Mazhar M, Aziz T, et al. HPLC, FTIR and GC-MS Analyses of Thymus vulgaris Phytochemicals Executing In Vitro and In Vivo Biological Activities and Effects on COX-1, COX-2 and Gastric Cancer Genes Computationally. Molecules. 2022;27:8512. https://doi.org/10.3390/molecules27238512.

127. Danduprolu J, Lalitha C. Phytochemistry and Antibacterial Potentiality of Selected Mangrove Plants from Coringa Wild Life Sanctuary, Andhra Pradesh, India. International Journal of Environmental Sciences. 2024;:1102–22. https://doi.org/10.64252/jsnzse22.

128. Lee J, Beers JL, Geffert RM, Jackson KD. A Review of CYP-Mediated Drug Interactions: Mechanisms and In Vitro Drug-Drug Interaction Assessment. Biomolecules. 2024;14:99. https://doi.org/10.3390/biom14010099.

129. May M, Schindler C. Clinically and pharmacologically relevant interactions of antidiabetic drugs. Ther Adv Endocrinol Metab. 2016;7:69–83. https://doi.org/10.1177/2042018816638050.

130. El Mehdi K, Khedraoui M, Bouribab A, Guerguer FZ, Errougui A, Chtita S. Discovery of Novel Dual EGFR/HER2 Inhibitors Using Integrated Docking, Molecular Dynamics, and MMGBSA Computational Approaches. ChemistrySelect. 2025;10:e01410. https://doi.org/10.1002/slct.202501410.

131. Ndarawit W, Ochieng CO, Angwenyi D, Cruz JN, Santos CBR, Kimani NM. Discovery of α-amylase and α-glucosidase dual inhibitors from NPASS database for management of Type 2 Diabetes Mellitus: A chemoinformatic approach. PLOS ONE. 2024;19:e0313758. https://doi.org/10.1371/journal.pone.0313758.

132. Febriyanti RM, Indradi RB, Maisyarah IT, Iskandar Y, Susanti RD, Lestari D. Alpha-amylase and Alpha-glucosidase enzymes inhibition and antioxidant potential of selected medicinal plants used as anti-diabetes by Sundanese community in West Java, Indonesia. BMC Complement Med Ther. 2025;25:426. https://doi.org/10.1186/s12906-025-05144-x.

Supplementary Information

Additional file 1. [PDF] **Title:** Supplementary experimental data. **Description:**

Figure SF1: Gallic acid calibration curve for total phenolic content (TPC). **Figure SF2:** Gallic acid calibration curve for total tannin content (TTC). **Figure SF3:** Quercetin calibration curve for total flavonoid content (TFC). **Table ST1:** Antioxidant activity of the methanolic extract of *H. fomes* leaves (MEHFL) in DPPH free radical scavenging assay. % Inhibition = $\frac{(Absorbance_{Negative\ control} - Absorbance_{Test\ sample})}{(Absorbance_{Negative\ control})} \times 100\ \%$; the negative control contained all reagents except the extract or ascorbic acid, while the test sample consisted of the reaction mixture containing either MEHFL or ascorbic acid. Results are expressed as mean ± SEM (n = 3). **Table ST2:** Ferricyanide reducing power of the methanolic extract of *H. fomes* leaves (MEHFL). Results are expressed as mean ± SEM (n = 3). **Table ST3: ST3:** Anti-inflammatory activity of the methanolic extract of *H. fomes* leaves (MEHFL) in bovine serum albumin (BSA) denaturation assay. % Inhibition = $\frac{(Absorbance_{Test\ sample} - Absorbance_{Negative\ control\ })}{(Absorbance_{Negative\ control})} \times 100\ \%$; the negative control contained all reagents except the extract or aspirin, while the test sample consisted of the reaction mixture containing either MEHFL or aspirin. Results are expressed as mean ± SEM (n = 3). **Table ST4:** Egg albumin denaturation activity of the methanolic extract of *H. fomes* leaves

(MEHFL) in egg albumin denaturation assay. % Inhibition = $\frac{(Absorbance_{Test\ sample} - Absorbance_{Negative\ control})}{(Absorbance_{Negative\ control})} \times 100\ \%$; the negative control contained all reagents except the extract or diclofenac, while the test sample consisted of the reaction mixture containing either MEHFL or diclofenac. Results are expressed as mean ± SEM (n = 3). **Table ST5:** α-amylase inhibitory activity of the methanolic extract of *H. fomes* leaves (MEHFL) in α-amylase inhibition assay. % Inhibition = $\frac{(Absorbance_{Negative\ control} - Absorbance_{Test\ sample})}{(Absorbance_{Negative\ control})} \times 100\ \%$; the negative control contained all reagents except the extract or acarbose, while the test sample consisted of the reaction mixture containing either MEHFL or acarbose. Results are expressed as mean ± SEM (n = 3). **Table ST6:** α-glucosidase inhibitory activity of the methanolic extract of *H. fomes* leaves (MEHFL) in α-glucosidase inhibition assay. % Inhibition = $\frac{(Absorbance_{Negative\ control} - Absorbance_{Test\ sample})}{(Absorbance_{Negative\ control})} \times 100\ \%$; the negative control contained all reagents except the extract or acarbose, while the test sample consisted of the reaction mixture containing either MEHFL or acarbose. Results are expressed as mean ± SEM (n = 3). **Table ST7:** Effects of the different concentrations of the methanolic extract of *H. fomes* leaves (MEHFL) in brine shrimp lethality bioassay. % Mortality = $\frac{(Total\ Nauplii - Alive\ Nauplii)}{(Total\ Nauplii)} \times 100\ \%$. Results are expressed as mean ± SEM (n = 3). **Table ST8:** Observations and appearance of MEHFL (methanolic extract of *H. fomes* leaves) and control groups during 14-day study period. (N. O = Not observed). **Table ST9:** Changes in body weight (g) of mice during the acute oral toxicity study of the methanolic extract of *H. fomes* leaves (MEHFL). Here W0, W1, and W2 represents day 0, 7 and 14 respectively. Data are represented as mean ± SEM (n = 5). **Table ST10:** Effect of the methanolic extract of *H. fomes* Leaves (MEHFL) on blood glucose levels in mice during the Oral Glucose Tolerance Test. Data are presented as mean ± SEM (n = 5). Statistical significance was

determined by one-way ANOVA followed by Dunnett post hoc test, where *, **, and *** indicate $p < 0.05$, 0.01, and 0.001 versus the negative control, and (a), (b), and (c) indicate $p < 0.05$, 0.01, and 0.001 versus the positive control. Here, AUC = Area under the curve. **Table ST11:** Effect of the methanolic extract of *H. fomes* Leaves (MEHFL) on fasting glucose levels (FBG) in alloxan induced diabetic rats during the 21 days study period. Data are presented as mean ± SEM (n = 5). Statistical significance was determined by one-way ANOVA followed by Dunnett post hoc test, where *, **, and *** indicate $p < 0.05$, 0.01, and 0.001 versus the negative control, and (a), (b), and (c) indicate $p < 0.05$, 0.01, and 0.001 versus the positive control. Here, AUC = Area under the curve. **Table ST12:** Secondary metabolite profile of the methanolic extract of *H. fomes* Leaves (MEHFL) identified via GC–MS analysis. (RT = Retention time)

Additional file 2. [PDF] **Title:** Supplementary in silico data. **Description:**

Figure SF4: PROCHECK Ramachandran plots of (A) α amylase, (B) α glucosidase. **Figure SF5:** ProSA-Web validation parameters of the target proteins. (A, B) Z scores of α amylase and α glucosidase within the range of experimentally determined NMR structures; (C, D) residue wise energy profiles of α amylase and α glucosidase, respectively. **Figure SF6:** PrankWeb predicted active site of (A) α amylase, (B) α glucosidase. **Figure SF7:** Molecular surface area (MolSA) and polar surface area (PSA) profiles of selected GC–MS identified compounds from the methanolic extract of *H. fomes* leaves (MEHFL). (A, B) MolSA in α amylase and α glucosidase, respectively; (C, D) PSA in α amylase and α glucosidase, respectively. **Table ST13:** General information of the ligand library for the computational analysis. **Table ST14**: Predicted binding pockets of the target proteins identified using the PrankWeb tool. **Table ST15:** Results of molecular docking of shortlisted GC–MS-identified compounds from the methanolic extract of *H. fomes* leaves (MEHFL) against both target proteins. **Table ST16:** Non-bond interaction profiles of the shortlisted GC–MS-guided compounds from the methanolic extract of *H. fomes* leaves (MEHFL) with α-amylase and α glucosidase. **Table ST17:** Comprehensive ADMET profile of shortlisted GC–MS identified compounds from the methanolic extract of *H. fomes* leaves (MEHFL). Abbreviation: HOB20%: Human oral bioavailability 20% (Probability), HOB50%: Human oral

bioavailability 50% (Probability), HIA: Human Intestinal Absorption, PGI: P−glycoprotein inhibitor, PGS: P−glycoprotein substrate, BBB: Blood−Brain barrier (Probability), FU: Fraction unbound (Human) (Percentage), PPB: Plasma protein binding (Percentage), VDss: Steady state volume of distribution (Log VDss), CYP1A2I: CYP 1A2 Inhibitor, CYP1A2S: CYP 1A2 Substrate, CYP2C19I: CYP 2C19 Inhibitor, CYP2C19S: CYP 2C19 Substrate, CYP2C9I: CYP 2C9 Inhibitor, CYP2C9S: CYP 2C9 Substrate, CYP2D6I: CYP 2D6 Inhibitor, CYP2D6S: CYP 2D6 Substrate, CYP3A4I: CYP 3A4 Inhibitor, CYP3A4S: CYP 3A4 Substrate, OATP1B1, OATP1B3, Cl: Clearance (ml/min/kg), OCT2: Organic cation transporter 2, HL: Half−life (hr), LD_{50}: LD_{50} (mg/kg), TC: Toxicity Class, Hep: Hepatotoxicity, Car: Carcinogenicity, Mut: Mutagenicity, Cyt: Cytotoxicity, B: Bioavailable, NB: Non-Bioavailable, NI: Non-Inhibitor, NS: Non-Substrate, I: Inhibitor, S: Substrate. **Table ST18:** Predicted passive permeability profiles of shortlisted GC–MS identified compounds from the methanolic extract of *H. fomes* leaves (MEHFL) obtained using the PerMM web tool. **Table ST19:** Predicted off targets (top 10) of the selected GC–MS identified compounds from the methanolic extract of *H. fomes* leaves (MEHFL) from SwissTargetPrediction.

Supplementary Files

This is a list of supplementary files associated with this preprint. Click to download.

- Additionalfile1Supplementaryexperimentaldata.pdf
- Additionalfile2Supplementaryinsilicodata.pdf